A tsunami generated by a strike-slip event: constraints from GPS and SAR data on the 2018 Palu earthquake

Wim Simons[1],Taco Broerse[2],Lin Shen[3],Olga Kleptsova[4],Nicolai Nijholt[1],Andrew Hooper[3],Julie Pietrzak[4],Yu Morishita[5],Marc Naeije[1],Stef Lhermitte[4],Matthew Herman[2],Dina Anggreni Sarsito[6],Joni Efendi[7],Sofian[8],Rob Govers[2],Christophe Vigny[9],Hasanuddin Zainal Abidin[6],Gatot Haryo Pramono[7],Cahyo Nugroho[8],Pieter Visser[1],Riccardo Riva[4]

[1]Faculty of Aerospace Engineering, Delft University of Technology, Delft, The Netherlands
[2]Department of Earth Sciences, Faculty of Geosciences, Utrecht University, Utrecht, The Netherlands
[3]COMET, School of Earth and Environment, University of Leeds, United Kingdom
[4]Faculty of Civil Engineering and Geosciences, Delft University of Technology, Delft, The Netherlands
[5]Geospatial Information Authority of Japan, Japan
[6]Geodesy Research Group, Institute of Technology Bandung, Indonesia
[7]Center for Geodetic Control Network and Geodynamics, Geospatial Information Agency, Indonesia
[8]Meterology, Climatology and Geophyscial Agency, Indonesia
[9]Département Terre Atmosphère Océan, École Normale Supérieure, France

Key Points:

- New GPS observations as part of a geodetic solution for the full 3D onshore coseismic displacements of the 2018 Palu earthquake.
- Below Palu Bay we find a strong indication of dip-slip on a fault bend, agreeing with the notion of Palu Valley being a transtensional basin.
- A large part of the tsunami, both in terms of arrival times and runup heights, can be explained by coseismic slip.

Corresponding author: Taco Broerse, d.b.t.broerse@uu.nl

Abstract

A devastating tsunami struck Palu Bay in the wake of the 28 September 2018 M_w = 7.5 Palu earthquake (Sulawesi, Indonesia). With a predominantly strike-slip mechanism, the question remains whether this unexpected tsunami was generated by the earthquake itself, or rather by earthquake-induced landslides. In this study we examine the tsunami potential of the co-seismic deformation. To this end, we present a novel geodetic dataset of GPS and multiple SAR-derived displacement fields to estimate a 3D co-seismic surface deformation field. The data reveal a number of fault bends, conforming to our interpretation of the tectonic setting as a transtensional basin. Using a Bayesian framework, we provide robust finite fault solutions of the co-seismic slip distribution, incorporating several scenarios of tectonically feasible fault orientations below the bay. These finite fault scenarios involve large co-seismic uplift (>2 m) below the bay due to thrusting on a restraining fault bend that connects the offshore continuation of two parallel onshore fault segments. With the co-seismic displacement estimates as input we simulate a number of tsunami cases. For most locations for which video-derived tsunami waveforms are available our models provide a qualitative fit to leading wave arrival times and polarity. The modeled tsunamis explain most of the observed runup. We conclude that co-seismic deformation was the main driver behind the tsunami that followed the Palu earthquake. Our unique geodetic dataset constrains vertical motions of the sea floor, and sheds new light on the tsunamigenesis of strike-slip faults in transtensional basins.

Plain Language Summary

The 28th September Palu earthquake ruptured the Palu-Koro fault in NW Sulawesi, Indonesia, and was followed by a devastating tsunami in Palu Bay. As the Palu-Koro fault accommodates mostly horizontal motion, many studies proposed that sub-marine landslides, rather than the earthquake itself, triggered the tsunami. This study focuses on the contribution of the earthquake to sea floor displacements. We present a unique geodetic dataset and estimate a high-resolution 3D displacement field. The rupture is not a straight feature in the landscape, but rather contains bends. It is near those bends that significant vertical displacements occurred. From the onshore geodetic data we infer another fault bend below Palu Bay. Estimations of fault slip for several scenarios of offshore fault geometries point to a few meters of sea floor uplift. We use these slip models as input for tsunami models, and can qualitatively explain the observations of tsunami runup heights and video-based tsunami arrival times around Palu Bay. Only at a few locations our models cannot explain tsunami observations, which leaves open the contribution of other possible sources to the tsunami locally. The Palu case underlines the potential importance of fault bends to tsunami generation for similar tectonic settings around the world.

1 Introduction

The 28 September 2018 Palu $M_w = 7.5$ earthquake ruptured the Palu-Koro strike-slip fault in northwestern Sulawesi (USGS, 2018) (Figure 1). The event was quickly followed by tsunami waves that first arrived 2-5 minutes after the rupture (Yalçıner et al., 2018; Takagi et al., 2019; Carvajal et al., 2019). Tsunami waves hit the coast of Palu Bay, but areas north of the bay, along the Makassar Strait, were hardly affected (Yalçıner et al., 2018; Omira et al., 2019), even though these areas are at comparable distances to the rupture. The unexpected amplitude of the tsunami and the timing of the earthquake increased the damage and may have caused additional casualties; the earthquake occurred at sunset when many people were present on the beach, at rising sea tide (at 80% of high tide, about 0.85 m). Furthermore, there have been numerous reports of landslides directly at the coast (Omira et al., 2019; Takagi et al., 2019; Liu et al., 2020), while liquefaction-induced landslides in Palu Valley destroyed suburban areas (Bradley et al., 2019; Watkin-

son & Hall, 2019). From a tsunami-generation perspective, an important question quickly arose: was the tsunami a result of co-seismic displacements of the sea floor, or did secondary effects such as (sub-marine) landslides play a major role (Arikawa et al., 2018; Muhari et al., 2018)?

The Palu-Koro fault, which runs underneath the city of Palu, accommodates approximately 4 cm/yr left-lateral relative plate motion (Walpersdorf, Rangin, & Vigny, 1998; Stevens et al., 1999; Bellier et al., 2001). However, interseismically the segment at Palu Bay and Valley is locked at shallow depths (down to 12 km), as indicated by GPS-derived velocities across the Palu-Koro fault (Walpersdorf, Vigny, et al., 1998; Socquet et al., 2006). This results in a steady accumulation of slip deficit. It was therefore clear that Palu is situated in an area with a high seismic hazard (Cipta et al., 2017; Watkinson & Hall, 2017). Geological (Bellier et al., 2006), geomorphological (Bellier et al., 1998, 2001) and geodetic observations (Walpersdorf, Vigny, et al., 1998; Socquet et al., 2006) clearly indicate that the Palu-Koro fault is an active fault system, even though seismological observations for a high-magnitude rupture are lacking (Watkinson & Hall, 2017). Pelinovsky et al. (1997) and Prasetya et al. (2001) attributed three tsunamis hitting Sulawesi's west coast over the last century to earthquakes in the Palu-Koro zone, even though the inferred source mechanisms indicated thrust and normal earthquakes rather than strike-slip.

The Quaternary activity of the prominent Palu-Koro fault is characterized in the geomorphology by very narrow, steep valleys as the fault runs through central Sulawesi (Katili, 1970; Bellier et al., 1998). The Palu-Koro fault system branches out at the surface, entering Palu Valley from the south, as it continues towards Palu Bay as a transtensional system; steep, valley-dipping normal faults bound the valley at the base of the surrounding mountain systems (Bellier et al., 1998; Watkinson & Hall, 2017). The transtensional nature of the Palu-Koro fault indicates the possibility for dip-slip components that increase vertical surface displacements during earthquakes, similar to what has been proposed for the Sea of Marmara region of the North Anatolian fault (Tinti et al., 2006). This may allow for large tsunami amplitudes during strike-slip earthquakes while the dominant motions are expected to be horizontal.

Seismological studies inferred that the $M_w = 7.5$ rupture started 72 km north of Palu (USGS, 2018), and propagated southwards at supershear velocity (i.e. faster than the shear wave velocity of the crust) (Bao et al., 2019). The seismologically inferred slip type is predominantly strike-slip but with a distinct dip-slip contribution, and peak slip has been mapped close to the surface (USGS, 2018; Yolsal-Çevikbilen & Taymaz, 2019; Li et al., 2020). Optical satellite data (Sotiris et al., 2018; Socquet et al., 2019) indicate that the southern part of the rupture reached the surface, and ran parallel with the fault traces as mapped prior to the earthquake (Watkinson & Hall, 2017; Wu et al., 2020). Contrastingly, north of Palu Bay these satellite data indicate a north-south oriented rupture through the Sulawesi Neck that does not follow a previously mapped major fault, as the northern continuation of the Palu-Koro fault was considered to continue offshore (Figure 1) (e.g., Bellier et al. (2001)).

Observations of the time evolution of the tsunami are sparse; there is only a single direct measurement of sea level at the tide gauge in Palu Bay, complemented by analyses from tsunami videos and interviews with witnesses (Yalçıner et al., 2018; Takagi et al., 2019). Both eyewitness accounts as well as video analyses (Carvajal et al., 2019) indicate a complex tsunami evolution, with multiple waves arriving from different directions. As an embayment like Palu Bay has the potential to produce reflected tsunami waves, it is inherently difficult to discern whether all observed tsunami fronts are generated by reflection of one major, tectonically induced tsunami, or whether multiple landslides are simultaneously producing waves. Surveys of inundation and runup heights suggest short wavelength tsunamis as runup distances are relatively short (Omira et al., 2019; Putra et al., 2019; Switzer et al., 2019). Multiple studies reported evidence for the oc-

currence of sub-marine landslides along the Bay coast (Arikawa et al., 2018; Omira et al., 2019; Takagi et al., 2019; Sassa & Takagawa, 2019) and their significance for generating tsunami waves in the bay (Pakoksung et al., 2019; Sepúlveda et al., 2020; Williamson et al., 2020; Schambach et al., 2020). Still, only for a few locations along the bay it has been possible to detect likely sources from bathymetry changes and put quantitative constraints on the displaced volumes (Liu et al., 2020). Many of the aforementioned studies have advocated for a dominant contribution of submarine landslides in generating the tsunami after the earthquake. Yet, due to a lack of accurate geodetic constraints, such as co-seismic GPS displacements, the offshore co-seismic displacement and its impact on generating tsunami waves have not been well constrained. The open question is still: can we find a geologically acceptable faulting model that agrees with observed surface deformation, and that also reproduces the tsunami observations without additional landslides?

To answer this question, we present a novel dataset of co-seismic GPS displacements combined with a large set of Synthetic Aperture Radar (SAR) pixel offsets and SAR interferometry (InSAR) to resolve simultaneously the near and far field surface displacements associated with the M_w 7.5 Palu earthquake. Our combination of geodetic observations yields improved constraints on the co-seismic 3D displacement field; especially the vertical surface motions are much better determined compared to previous studies that relied on InSAR or optical correlation displacements only (Socquet et al., 2019; Ulrich et al., 2019; Fang et al., 2019; Jamelot et al., 2019; Sepúlveda et al., 2020; Williamson et al., 2020). Using this extensive set of geodetic data, we estimate a robust finite fault solution of the co-seismic slip distribution in a Bayesian inversion. As parts of the fault run below Palu Bay, these are only observed indirectly. Hence, we test multiple scenarios of tectonically feasible orientations of fault segments running below the bay. We then perform forward tsunami models based on the finite fault scenarios, and examine those against the available tsunami timing and runup height observations. Thereby, our study aims at providing a better view on the role of co-seismic sea floor displacements in driving the devastating tsunami in Palu Bay.

2 Data

2.1 GPS network

Since the first campaign-style GPS surveys in Sulawesi for the 1994-1998 time window (Wilson et al., 1998), TU Delft and ENS, in corporation with the Badan Informasi Geospasial (BIG) and Institut Teknologi Bandung, have gradually densified the GPS monument network to $\sim$ 40 data points around the Palu-Koro fault and in North Sulawesi. The campaign stations have been surveyed on a yearly basis, and there are 5 continuous stations near the Palu-Koro fault. Before, during and after the $M_w = 7.5$ earthquake all 5 continuous GPS stations near the Palu-Koro fault were operational, collecting data at 30 or 1 s intervals. Many of the GPS points have been surveyed less than a year earlier in campaign-style, including 4 GPS points in Palu surveyed just 1.5 months prior to the earthquake. In the following 2-5 weeks after the earthquake, all available GPS campaign points (35) have been re-surveyed for at least 3 full days. Figure 1 shows the co-seismic displacements, computed using 1) high-rate kinematic GPS solutions (for continuous GPS with large displacements), 2) by differencing solutions spanning 12 days before and 12 days after the earthquake (for continuous sites with smaller displacements), and 3) by differencing multi-day averaged positions with extrapolated pre-earthquake positions corrected for linear velocities (campaign sites). Supplemental section 2 provides technical details, and all co-seismic offsets can be found in supplementary table S1.

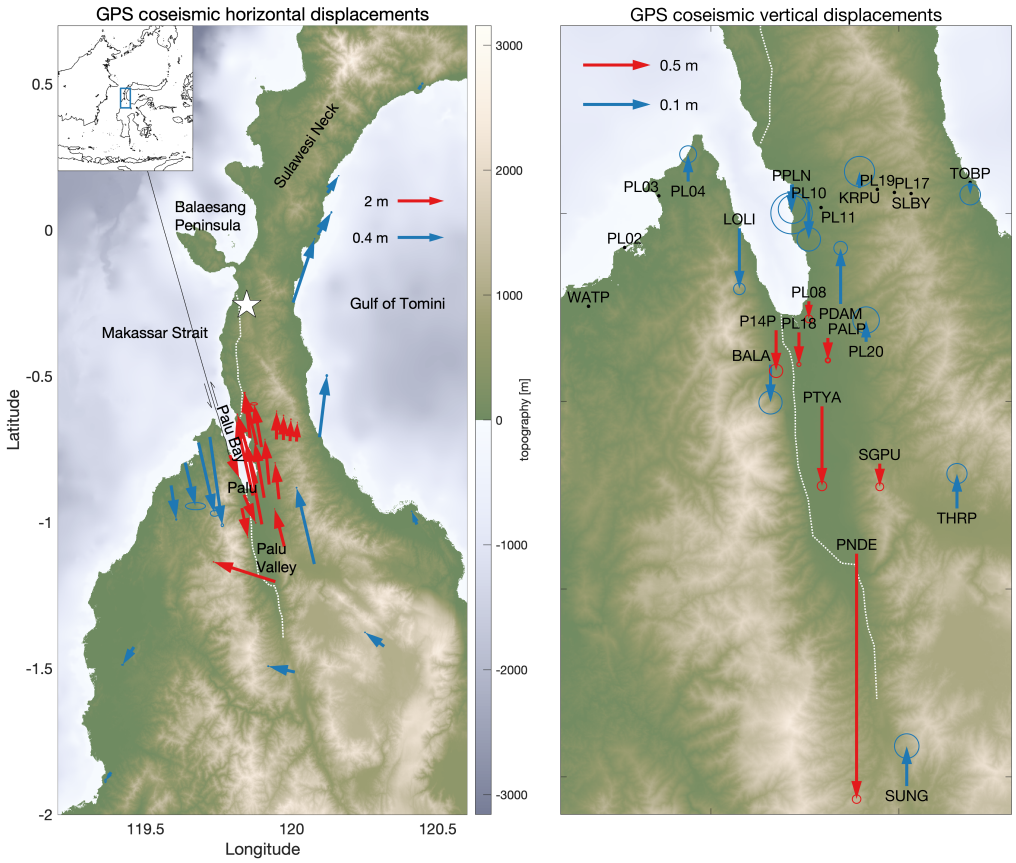

Figure 1. Left panel: horizontal GPS co-seismic displacements (with 95% confidence ellipses), topography, and onshore fault traces (dotted white line) as obtained from SAR data. The straight black line shows the continuation of the Palu-Koro fault as proposed in literature (e.g., Bellier et al. (2006)), but which deviates from the 2018 surface rupture. Right panel: vertical GPS displacements (with 95% confidence intervals shown as circles). Vertical displacements at sites below 2σ are not shown (black dots). We use a different scaling for the large displacements (red) and small displacements (blue), see the example vectors. All co-seismic offsets can be found in supplemental table S1.

2.2 SAR data processing

We apply InSAR, multiple aperture InSAR (MAI), and pixel-offset tracking to ALOS-2 SAR data in the L-band frequency range, to obtain a detailed co-seismic surface deformation field. The post-earthquake SAR data were acquired between 4 and 27 days since the event (see supplementary table S3). L-band SAR data is much more suitable than C-band for a vegetated area like Sulawesi, in terms of coherence (e.g., Rosen et al. (1996)). Each of these techniques observes different components of the displacement field, and has its own strengths and weaknesses. InSAR reveals line-of-sight deformation with high precision, but it has almost no sensitivity to deformation in the north-south direction, due to a near-polar orbit. Furthermore, InSAR tends to be decorrelated in the areas of large displacement; as figure 2 shows, there are gaps for InSAR for most areas adjacent to the rupture, both in the Sulawesi Neck and Palu Valley. In contrast, MAI gives displacement along track and is mostly sensitive to deformation in the north-south direction, although its precision is lower than that of InSAR (Bechor & Zebker, 2006; Jung et al., 2009). Pixel-offset tracking has a lower precision still, but provides estimates of deformation in both the line-of-sight and along-track directions, even in areas of large deformation (Michel et al., 1999; Tobita et al., 2001). We use a pair of ScanSAR data and four pairs of Stripmap data to cover the whole deformation area from both ascending and descending orbits (Supplementary table S3). We downsample the processed SAR-derived data set using quadtrees (Decriem et al., 2010) and estimate errors for each data set by computing 1-D semivariograms (Bagnardi & Hooper, 2018) over the non-deforming regions (see supplementary section 3.1). The lower panel of figure 2 shows the different levels of uncertainty of the used SAR products, which also agree well with the level of misfit with the (projected) GPS observations. Combined, these SAR products provide a complete view of the 3D co-seismic displacement field. Lower precision techniques prove useful as these cover the regions with large displacements on the order of meters, near the surface rupture, where InSAR lacks a solution.

2.3 Estimation of 3D displacements

The multiple SAR-derived displacements fields have highly complementary sensitivities to all directions of the displacement field, but are difficult to interpret simultaneously. Therefore, we estimate a continuous 3D displacement field from the SAR displacement fields to combine the different looking directions, while the GPS data serve to remove offsets and linear trends in the SAR displacements. We invert for the north, east and up displacements and linear trends in the SAR displacements unrelated to the co-seismic deformation, on a triangular mesh in a single linear least squares inversion, similar to H. Wang and Wright (2012). To incorporate the SAR fields in the inversion, we construct Green's functions that relate surface displacement to the SAR observation direction (Wright et al., 2004). We increase the local influence of the GPS data using spatial smoothing, by including a Laplacian operator in the inversion. The variable mesh size follows the spatial variability of the SAR displacements, and as we apply the same amount of smoothing between all neighboring mesh elements, the relative smoothing is dominated by the spatial variability of the SAR displacement fields. In this way we make optimal use of the SAR spatial resolution. In supplementary section 4 we provide details on the inversion procedure, the effect of smoothing, and on the propagation of data uncertainties.

2.4 Displacement field

The combination of SAR and GPS data provides a consistent co-seismic displacement field, as depicted in figure 3, with residuals generally on the order of the data uncertainties (supplemental figure S8). We find good signal-to-noise ratios for the north and east displacements in the area of interest, and for the vertical displacements around the faults (see uncertainties in supplementary figures S4 and S5, that also show north

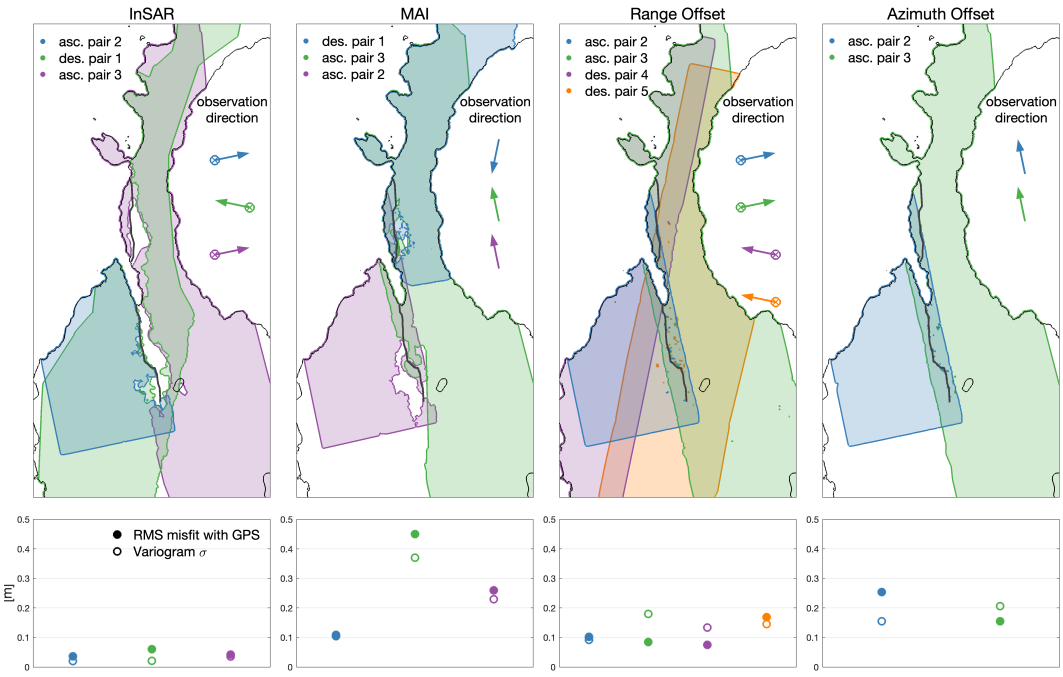

Figure 2. SAR data availability: areas covered by displacement fields from InSAR, MAI, and SAR range and azimuth offsets (asc: ascending orbits; des: descending orbits). Supplementary table S3 provides details on the ALOS-2 data used. The arrow indicates the observation direction, where a $\otimes$ denotes a vertical component (down looking) for InSAR and range offsets. The dark gray line depicts the surface trace. The lower panels indicate: the respective misfits with spatially overlapping GPS data, projected onto the same looking direction as the SAR data, and after removing an estimated offset ramp for the SAR fields, and the estimated standard deviation error, calculated for the SAR displacement field using semivariograms. We have estimated semivariograms for each SAR displacement field in areas unaffected by co-seismic displacements, hence the semivariogram standard deviation σ should be indicative for the noise level of each SAR product. For the computation of the RMS misfit with the GPS data, misfits larger than 2 times the RMS are removed as outliers. Supplementary figure S13 shows all SAR-derived displacement fields.

.

and east displacements separately). Approximately north-south displacements along the main Palu fault are the dominant motions; the largest displacements occurred on the east side of the fault in Palu Valley, see label (a) in figure 3. The displacement field shows a sharp discontinuity south of the Bay, with several meters of displacement east of the surface break, suggesting extensive shallow slip along the Palu Valley rupture segment. On the other hand, we find a gradual gradient in the left-lateral motion north of the Bay (b) up to the epicenter (mostly informed by the SAR azimuth offsets and MAI, see supplementary figure S13). Fault-perpendicular horizontal motions at the lateral ends of the rupture (c) indicate the expected quadrupole pattern of left-lateral slip, with minor patches of eastward motion east of the fault in Palu Valley (supplementary figure S4). The near-field vertical displacements are small in general, on the order of a few tens of cm. Only around the restraining fault bend (d) in southern Palu Valley co-seismic subsidence exceeds 1 meter. Similarly, we find local areas with uplift at the locations where we infer right-stepping fault bends in the Sulawesi Neck, north of the Bay (e). For a left-lateral fault system, the subsidence is in agreement with extension on a dilatational (releasing) fault bend while the uplift agrees with compressional (restraining) fault bends (Oglesby, 2005). For a graphical explanation of restraining and releasing fault bends, see figure 4. Around Palu City we observe only small subsidence values on the order of ~ 20 cm (e.g. site *PL18*, see table S1), and this general subsidence of a few decimeter applies to most of Palu Valley (f). Subsidence and NNW motion in the Sulawesi Neck (g) suggest normal faulting east of the main fault. Around the northern end of the onshore part of the fault (h) we obtain widespread subsidence.

3 Transtension in the Palu-Koro fault region of NW Sulawesi

The tectonic setting of Palu Valley and Bay

The Palu-Koro fault is a mature strike-slip fault as it has accommodated up to 150-250 km of left-lateral motion since the end of the Miocene (Bellier et al., 2006; Walpersdorf, Rangin, & Vigny, 1998). Mature strike-slip faults commonly display complex structural features in the upper crust overlying a single, planar strike-slip fault at depth, thereby deviating from the concept of a single fault place cutting the entire lithosphere (Tchalenko, 1970). Indications that the Palu-Koro fault is structurally complex are: 1) the maturity of the fault system, evidenced by the rectilinear geometry of the Palu Valley and Bay (graben-like) depression, sitting in between two mountain ranges with peaks >2 km (Abendanon, 1915; Katili, 1970), 2) the presence of large vertical offsets on steep valley-dipping faults, which display notable strike-slip displacements (Katili, 1970; Bellier et al., 1998; Watkinson & Hall, 2017; Patria & Putra, 2020), 3) an onshore releasing bend (indicated by *d* in figure 3), as well as an offset between the fault trace north and south of the bay during the co-seismic rupture.

These geological observations must be taken into account when considering a co-seismic slip distribution on a finite fault plane. Namely, the observed surface deformation field (figure 3) is only constrained on land, and therefore cannot be directly used to understand the tsunami. The geology suggests that the offset between the fault trace north and south of the bay may be due to a fault bend inside the bay. As this potential fault bend would be right-stepping within the left-lateral Palu fault it will be a transpressional structure, in an overall transtensional setting. We aim to develop a physical fault model that reproduces the observations plus the seismic moment tensor. Surface faulting does not necessarily continue in the subsurface with the same fault orientation, so that we need to tailor our finite fault model to the tectonic setting of Palu Valley and Bay. Lacking direct seismic profiles across the Palu-Koro fault, we consider fault structures in similar geological settings worldwide.

Often, strike-slip faults are characterized by a system of continuously developing Riedel shear faults at the surface, rather than a single straight fault trace (Tchalenko,

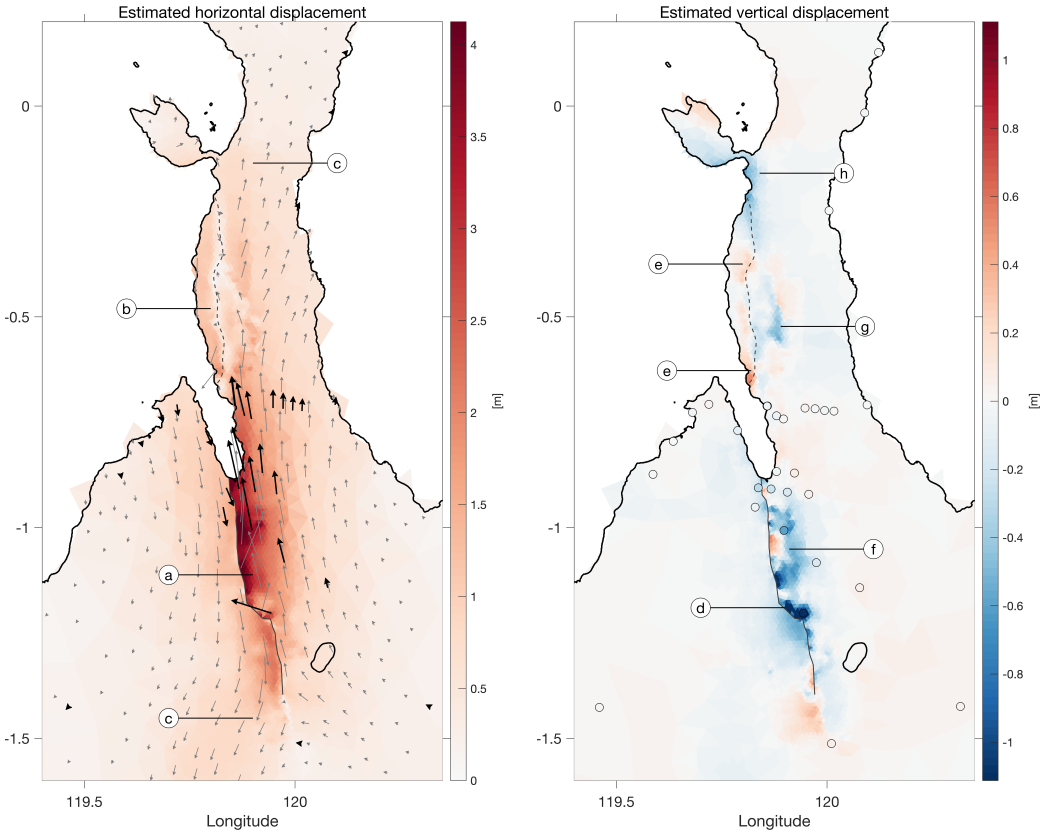

Figure 3. Estimated surface displacements, inverted from SAR and GPS displacements. Left panel: horizontal displacements, with observed GPS vectors in black. Right panel: estimated vertical displacements, with uplift defined as positive. Circles denote GPS sites, where the color shows the observed vertical displacements. Black continuous line shows the surface rupture in Palu Valley, the dashed line shows the presumed surface trace north of the bay, following the gradual transition from southwards to northwards deformation. Notable features: a, sharp transition in north-south displacements in Palu Valley; b) smooth transition in north-south displacements showing an absence of localized surface rupture; c) east-west displacements consistent with the ends of a left-lateral strike-slip rupture; d) subsidence at a southern releasing fault bend; e) uplifting areas consistent with compressional fault bends; f) general subsidence in Palu Valley; g) displacements suggesting normal faulting parallel to the main rupture; h) subsidence at the west coast of the Sulawesi Neck. Supplementary figures S4 and S5 contain the uncertainties of the displacement fields. We fit the GPS displacements well within the observation uncertainties, see supplemental figure S6.

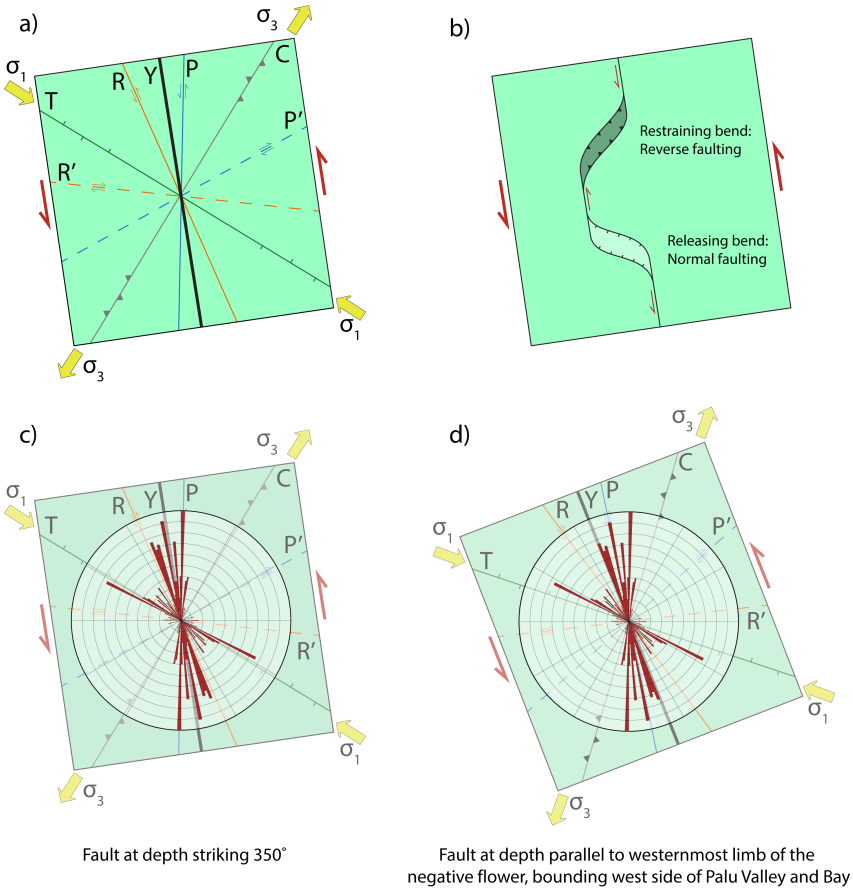

Figure 4. Interpretation of fault strikes in the 2018 rupture area as Riedel shears. (Upper left) Schematic illustration of subsidiary faults in a left-lateral shear zone. With respect to an underlying main shear zone or fault (Y), Riedel shears form at fixed orientations: ∼15 degrees for R shears, and ∼75 degrees for R' shears (Tchalenko, 1970). The minor P and antithetic P' shears are oriented approximately symmetric across the main fault compared to the R and R' shears. Tensional (T) and compressive (C) faults arise perpendicular to the positive (σ_3) and negative (σ_1) horizontal stress directions, respectively. (Upper right) Schematic illustration of azimuthal bends of the main fault in the along-strike direction. Relative motion causes a releasing bend with normal faulting and basin formation, or a restraining bend with reverse faulting (i.e. thrusting) and local uplift (Crowell, 1974). (Lower left) Rose diagram of the strikes of the active fault trace from the 2018 rupture and other features in the structural geology of the Palu-Koro fault region (Bellier et al., 1998, 2006; Leeuwen & Muhardjo, 2005; Hennig et al., 2017; Watkinson & Hall, 2017; Jaya et al., 2019; Natawidjaja et al., 2020) overlying the Riedel shear system of a main fault striking ∼350 degrees. (Lower right) The same rose diagram overlying a system of Riedel shear fault orientations where the main fault runs parallel to the easternmost limb of the negative flower structure (i.e., approximately parallel to the western coast of Palu Bay, striking ∼340 degrees).

1970). The upper left panel of figure 4 shows such a generic set of subsidiary faults that accommodate strain within a fault zone. Such a set is comprised of subsidiary faults that accommodate strain within the fault zone, and is comprised of several fault types (R, R', P, T, C) with distinct orientations and relative motions with respect to the main fault/shear zone at depth (Y). Figure 4, upper right panel, displays the potential development of releasing bends (resulting in extension due to normal faults) or restraining bends (resulting in shortening due to reverse faults) in case the main fault trace locally changes strike (Crowell, 1974).

Releasing bends can lead to the formation of a transtensional basin, where faults may form a negative flower structure when observed in a vertical cross-section (Harding, 1985). The subsiding basin that centers the shallow section of the negative flower structure is bound by faults that dip steeply at the surface. The relative displacement on these faults can be both normal and strike-slip. The dip angle changes with depth for many of these faults such that faults that are parallel at the surface converge at depth to a subvertical, deeper main fault (Harding, 1985). Previously, Watkinson and Hall (2017) argued for such a straight, cross-basin fault at depth for Palu Valley. Various splay faults thus reach the surface from a single, buried, main fault that is continuous at depth, whilst the shallow architecture of a transtensional basin may be very complex (Aksu et al., 2000; Laigle et al., 2008). We summarize in figure 5 our interpretation of the Palu-Koro fault as a transtensional basin, characterized by a negative flower structure in the Palu Valley and Bay region.

Interpretation of fault orientations as Riedel shears

Surface-breaking faults of a negative flower structure do not have to trace the strike of buried main faults in transtensional basins strictly, as is the case in the Sea of Marmara (Aksu et al., 2000; Yalçıner et al., 2002; Laigle et al., 2008). Hence, we interpret surface faults as being consistent with Riedel shear orientations (upper left panel of figure 4), linked to an underlying fault. We take the strikes of the fault structures traced from the 2018 fault rupture and other features in the structural geology of the Palu-Koro fault region between 0.12N and -1.27S (Bellier et al., 1998; Leeuwen & Muhardjo, 2005; Watkinson & Hall, 2017; Natawidjaja et al., 2020). In the lower panels of figure 4 we compare these fault strikes with the subsidiary fault orientations of a Riedel shear system (Tchalenko, 1970) considering two scenarios: a main fault striking ∼350 degrees, and a main fault that strikes parallel to the previously hypothesized main fault that bounds the west side of Palu Valley and Bay at ∼340 degrees (e.g., Walpersdorf, Vigny, et al. (1998); Bellier et al. (2001, 2006); Natawidjaja et al. (2020)). Both these options fall within the observed maximum horizontal stress directions (Heidbach et al., 2018). Only a main fault striking at 350 degrees leads to a Riedel shear system that is in agreement with the observed fault distribution in the deformation zone of the Palu-Koro fault, leading to a distinctly more northward rather than NNW orientation. In our interpretation, illustrated by figure 5, the west side of Palu Valley and Bay would be a Riedel shear (R) and the outer limb of the negative flower. The east side of Palu Valley and Bay denote more distributed deformation, with multiple discontinuous fault strands.

We find orientations of normal faults (T) in the Riedel shear system at releasing bends at the southern entrance of Palu Valley and within Palu Bay, along the eastern side of Palu Valley and just offshore Balaesang Peninsula (Natawidjaja et al., 2020). In our interpretation, the deep continuation of the Palu-Koro fault strikes away from the west side of the Palu Valley and Bay, and runs beneath the Sulawesi Neck instead, just east of Palu Bay. The 2018 rupture started above this hypothesized deep segment below the Sulawesi Neck, and only south of Palu Bay follows the western faults of the Palu-Koro fault system.

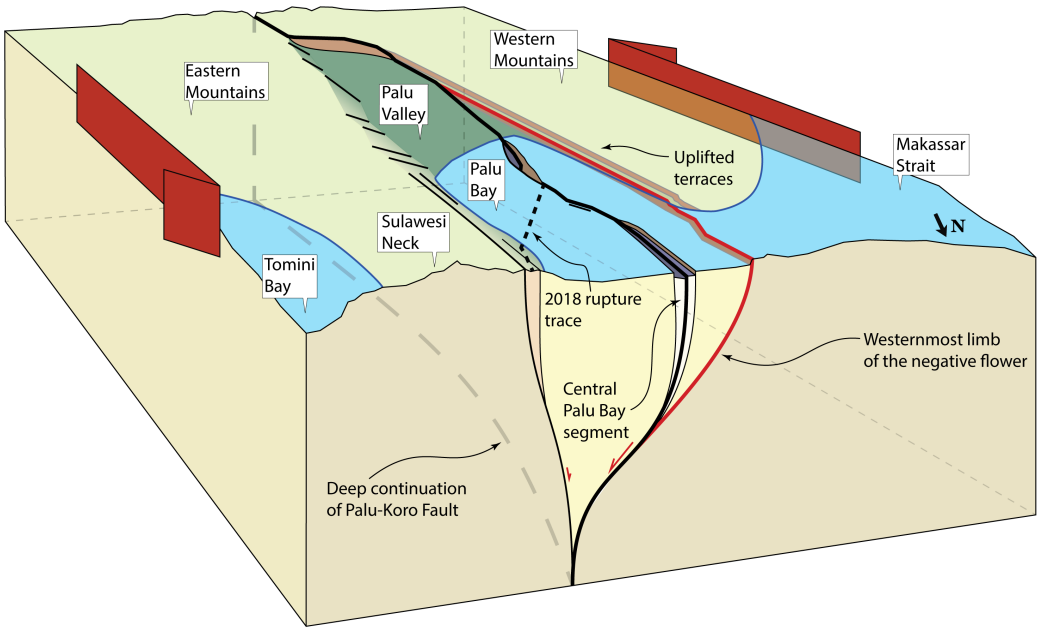

Figure 5. Synoptic view of the transtensional setting (i.e., a combination of strike-slip and normal faulting) of the Palu-Koro fault in the Palu Valley and Palu Bay region, using the active fault trace from the 2018 rupture and other features in the structural geology (Bellier et al., 1998, 2006; Leeuwen & Muhardjo, 2005; Hennig et al., 2017; Watkinson & Hall, 2017; Jaya et al., 2019; Natawidjaja et al., 2020). In our interpretation, the Palu Valley and Bay region is the downthrown part of a negative flower structure; the westernmost limb runs along the west side of Palu Valley and Bay (red line) with many offset terraces, streams and cut alluvial fans and the largest normal motion (Bellier et al., 1998, 2001, 2006; Watkinson & Hall, 2017; Patria & Putra, 2020). The eastern side of Palu Valley and Bay displays more distributed differential motion (Watkinson & Hall, 2017; Natawidjaja et al., 2020). The Central Palu Bay segment (Natawidjaja et al., 2020) appears relevant for the 2018 rupture trace only up to the point where the rupture changes strike abruptly towards the Sulawesi Neck, shown here with a dotted black line (see also figure 3). Below the bay, we expect a fault bend that connects the parallel fault strands north and south of the bay. Being a right stepping fault segment on a left-lateral strike slip fault, we foresee transpressional deformation (i.e., a combination of strike-slip and thrust faulting) on this restraining fault bend. In our interpretation, the main fault at depth has a strike of $\sim$ 350 degrees, up to the point where it leaves Palu Valley in the south, from where it changes strike southward. The vertical offsets have been exaggerated for visual purposes.

Transtensional basin structure of Palu Valley and Bay

A deep continuation of the Palu-Koro fault just onshore the eastern side of Palu Bay is also supported by pre-2018 inter-seismic displacements across the fault, as observed by the GPS transect of Socquet et al. (2006). Their fault model includes locking down to 12 km depth, and has a strike parallel to the previously discussed hypothesis of a main fault at the west side of the Bay, similar as Stevens et al. (1999). However, as GPS vector azimuths in Socquet et al. (2006) show a consistent clockwise misfit of 5-15 degrees, we suggest that a $\sim$ 350 degrees strike of the deep continuation of the Palu-Koro fault may solve these azimuthal misfits. We note that a structural interpretation of the Palu Valley and Bay (and further offshore) domain as a pull-apart basin (Natawidjaja et al., 2020) does not fit this geodetic observation, as this would require a northward continuation of the main, deep fault west of the Bay. Furthermore, a pull-apart basin does not match the subsidiary Riedel shear fault orientations well (lower right panel of figure 4). The hypocenter distribution beneath and offshore the Sulawesi Neck (Supendi et al., 2020) agrees with our structural interpretation of the transtensional basin system with (potential) activity on multiple fault strands (especially before the 2018 event). The post-earthquake seismicity does seem to show a preference to the Sulawesi Neck, surrounding our inferred main fault at depth.

The tectonic setting of strike-slip faults does not commonly lead to tsunamigenic earthquakes, due to the predominance of co-seismic surface motions in the horizontal plane. The transtensional nature of the Palu-Koro fault, with multiple fault segments at shallow levels, indicates the possibility for dip-slip components that enhance vertical surface displacements during earthquakes. The Palu-Koro fault thus hosts potential for localized vertical sub-marine motions able to generate tsunamis (similar to the cases described by Geist and Zoback (1999); Tinti et al. (2006)).

4 Fault slip and tsunami modelling

4.1 Fault model and inversion

We invert the observed surface displacements to constrain the co-seismic fault slip distribution. For the onshore part, the fault trace is clearly visible, as shown by figure 3, especially in Palu Valley (a similar inference has been made from optical data (Sotiris et al., 2018)), and that allows us to clearly define successive fault segments. Because we do not have direct observations of the course of the ruptured fault below the bay we consider multiple scenarios for fault geometries there. Modeling suggest that the presence of a fault bend that links the northern and southern segments increases the ability for the rupture to propagate (Oglesby, 2005). The displacement field at the location where the fault enters the bay suggests a strike change in the direction of the southern part of the fault (figure 3), which is in favor of a continuous rupture from north to south. Furthermore, the analysis by Biasi and Wesnousky (2016) of mapped surface ruptures indicates that an earthquake passing a >5 km step-over, as would result from a discontinuity between the northern and southern fault strands, is relatively rare for strike-slip. Nevertheless, we also test a scenario where we treat the rupture as discontinuous (e.g. Williamson et al. (2020)). In all cases, we are looking for a minimum-complexity fault model with a single fault strand, as the seismological moment tensor is a dominantly (90%) double couple (USGS, 2018). We treat the orientation of the connecting fault segments below the bay as a free parameter. Because we lack a priori information about the dip orientation of the ruptured fault, we solve for the dip angle of each segment in the inversion. As the fault likely has a negative flower structure (see figure 5 for a schematic representation), the dip angle is likely to change with depth. For the cross-basin deep fault (Watkinson & Hall, 2017) we assume a single deep fault that underlies the shallow fault segments, with an approximate 350 degree strike (see section 3). Two areas, distinct from the main strike-slip rupture, show notable subsidence and horizontal dis-

placement perpendicular to the main fault that we interpret as slip on normal faults: east of the main fault in the Sulawesi Neck (point g in figure 3) and northwest of the main fault in the Balaesang peninsula (as also proposed by Socquet et al. (2019)).

4.1.1 Fault segmentation and discretization

We use 16 fault segments to characterize the fault geometry; 13 segments belong to the main fault: A to M from the south to north, including four fault bend segments (B, H, I, and K) that differ in strike from the dominant north-south strike (left panel of figure 6). Segments F, G and H comprise the connection through Palu Bay, where F and H are partly onshore so that their strike angles are fixed based on the visible fault trace. Segment O represents the normal fault parallel to the main rupture; the fault in the Belaesang peninsula we model by segment N; the deep cross-basin fault by segment P. We subdivide the shallow segments (0 - 7 km depth) in multiple patches that increase in size with depth to impose increasing smoothness with depth; the cross-basin fault ranges from 7 to 22 km depth (see supplementary section 5 for more details).

4.1.2 Slip inversion

We apply a Bayesian approach that samples the posterior probability density function (PDF) of each model parameter through a Markov chain Monte Carlo (MCMC) scheme, incorporating an automatic step size selection (Bagnardi & Hooper, 2018). We use rectangular dislocation sources in an elastic half-space (Okada, 1985) with a Poisson's ratio of $\nu = 0.25$ and a shear modulus of 32 GPa. We solve for slip magnitude, in a 0-10 m range, and rake per patch, for which constraints are needed to avoid alternating slip directions from patch to patch. For the strike-slip segments we constrain the rake to be in the -20° to 20° range as we expect the rupture to be dominated by the left-lateral strike-slip. Right-stepping fault bends (H, I, K) have rake constraints of 0° to 90° (i.e. thrusting with a left-lateral component), while the left-stepping fault bends (B, N) and the parallel normal fault (O) have a -90° to 0° rake constraint (normal faulting with a left-lateral component), to reflect the expected compression and extension, respectively, for a left-lateral fault system.

We solve for the dip angle of each segment. The asymmetry of the displacements suggests east dipping faults, except for the most southerly segment A (figure 3). The minimum dip angle for strike-slip segments is 40° and 30° for the remaining segments. Segments F and H are continuations of onshore segments (E and I, respectively) and we solve for their endpoints below the bay; the length and orientation of segment G are thus (free) parameters, as this segment is entirely located offshore.

As the slip magnitudes of the deep patches are usually poorly constrained by the surface observations, changes in the slip magnitudes of the deep patches may not cause a large change to the posterior probability. Therefore, we apply a prior constraint on the seismic moment, assuming a Gaussian distribution with the mean from the USGS solution ($2.497{\cdot}10^{20}$ N$\cdot$m^{-1}) and a 10% standard deviation. Simultaneously we estimate a plane for the SAR-derived data to solve for reference errors. The inversion result consists of posterior probability density functions for all estimated parameters, based on a large set of tested fault slip solutions ($\sim$ 5 million), with a varying fit to the data.

4.1.3 Fault orientation below the bay: six model scenarios

Because there is no data that precisely locates the course of the rupture below the bay, we test different scenarios, shown in figure 6, which only differ with respect to the bay segments (i.e. F, G and H). Here, we vary the slip constraints and/or fault orientation between four different tectonically feasible scenarios. The shallow rupture below the bay may include left-lateral strike-slip faults as a continuation of the onshore faults, as well as a right-stepping fault bend to connect the parallel segments north and south

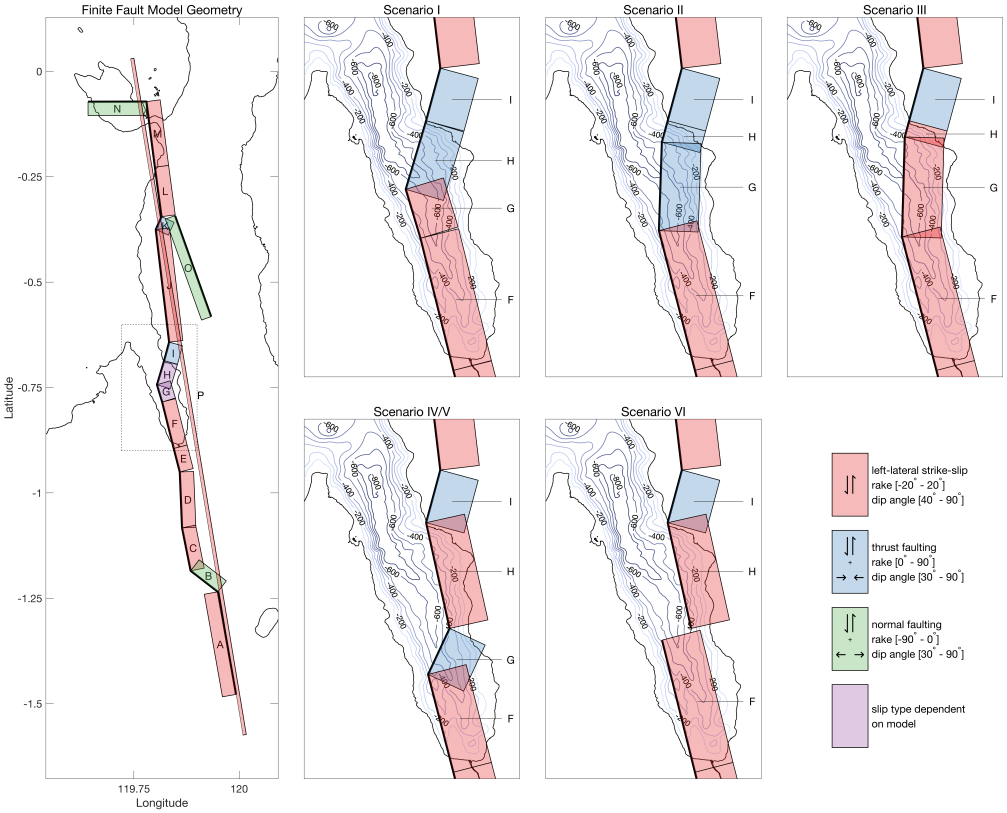

Figure 6. Fault model surface trace geometry. Left panel: fault discretization in segments and slip constraints. The rectangle depicts the bay section. Right panel: six model scenarios for the bay section of the rupture. Thick black line represents the segmentation of the fault trace. The shallow curved segments in figure 5 (red line) are represented in the model by planar planes with a dip angle that is consistent with the updip part of the flower structure, as this dip angle has the largest imprint on the surface displacements. Shallow segments A to O span depths between 0 - 7 km. The deep cross-basin fault P ranges between 7 - 22 km depth. Background: model bathymetry.

.

of the bay. In this context the fault bend would become a restraining bend, leading to a combination of left-lateral strike-slip and thrusting (i.e., transpression). In *Scenario I* we consider segment H to be the complete fault bend, implying dominant thrusting; segments F and G are forced to be strike-slip segments. Alternatively, to allow for a gradual strike change of the fault bend, in *Scenario II* we consider both H and G to be fault bends, and only F is considered strike-slip. *Scenario III* explores the possibility that all bay segments are dominantly strike-slip. Next, as some studies advocated for a tsunami source relatively far south in the Bay, based on tsunami arrival times at the Pantoloan tide gauge (Carvajal et al., 2019), we force the location of significant uplift, i.e. the fault bend, to be in the southern part of the Bay in *Scenario IV*. To do so, we set the middle segment G as the fault bend, while we set the northern and southern segments F and H as strike-slip in *Scenario IV*. We fix the length of the northern bay segment H at 10 km, such that the fault bend G situates at the 170 s travel time contour from Carvajal et al. (2019). *Scenario V* is a variation on the former, where the southern segment F has a free strike. As a last model we investigate a possible discontinuity in the rupture propagation, with no slip on the middle bay segment, resulting in a step-over between the two parallel fault segments H and F in *Scenario VI* (a setup previously explored by Williamson et al. (2020)). To suppress possible vertical motions within the 170 s travel time contour with respect to Pantoloan, we add quasi-observations of zero vertical displacement (with a standard deviation of 1 mm) above segment H in scenarios *IV, V* and *VI*.

4.1.4 Model initialisation

To cover a broad search space for the fault parameters that we aim to estimate, especially the fault geometry below the bay, we apply simulated annealing in the first steps of our inversion. We apply the simulated annealing approach (Van Laarhoven & Aarts, 1987) to scenarios *I, IV, V* and *VI* to test model parameters in a large search space. We then use the optimal solutions inverted from the simulated annealing as the initial solutions of the later Bayesian inversion for scenarios *I*, *IV, V* and *VI*, whereas the initial solutions of model scenarios *II* and *III* are adapted from the optimal (MAP) solution of the Bayesian inversion of scenario *I*.

5 Tsunami modeling and bathymetry

For the numerical simulation of the tsunami propagation and inundation we make use of an unstructured finite-volume model, H2Ocean (Cui et al., 2010, 2012). The model is based on the nonlinear shallow water equations discretized using a finite volume approach. H2Ocean preserves mass and momentum in local cells as well as maintaining the positivity of the water depth in the case of wetting and drying. The model was successfully used to simulate the evolution and maximum run-up and inundation height of the 2004 Indian Ocean Tsunami and 2011 Tohoku Tsunami (Cui et al., 2010; Hooper et al., 2013; Shimozono et al., 2014).

The combined DTM/Bathymetry grid for the tsunami modeling has an 8 m DTM resolution and 60 m bathymetry resolution, and is based on data provided by BIG (Badan Informasi Geospasial, Indonesia). We have calibrated both DTM and bathymetry to mean sea level (see supplementary section 7). The reported RMS error of the DTM is 2.79 m. We use a computational mesh, generated using OceanMesh2D (Roberts et al., 2019), with a 5-10 m resolution for the inundated area inside Palu Bay and the adjacent coastal area. We decrease the grid resolution gradually to 250 m close to the epicenter and down to 2.5 km in the Makassar basin west of Sulawesi.

The tsunami model is driven by instantaneous vertical displacements of the sea surface and bed. The effective vertical displacement is calculated following Tanioka and Sa-

take (1996):

$$d = -u_x \frac{\partial H}{\partial x} - u_y \frac{\partial H}{\partial y} + u_z \tag{1}$$

where u_x, u_y and u_z are the displacement components in east, north and up directions from the co-seismic slip model, respectively, and H is the bathymetry (defined here positive upward, hence the minus signs). Since the earthquake occurred close to the time of the high tide, the tidal elevation may contribute significantly to the tsunami inundation. Therefore, we set the initial still water level to 0.85 m, the tidal elevation level observed at the Pantoloan tide gauge just before the earthquake. We use a quadratic friction law with a Chezy coefficient of 0.003. The timesteps are variable and are determined by setting the Courant number to 0.8 (Cui et al., 2010).

We compare modeled tsunami elevations η with video waveforms derived by Carvajal et al. (2019), by computing the relative tsunami elevation, that takes into account the vertical displacement of a point of observation:

$$\eta_{\text{rel}} = \eta - u_z \tag{2}$$

whereas for computing inundation we update the bathymetry by d, the spatial vertical displacement. To compute inundation distance and runup height along the coastline (taken as the zero contour from the combined DTM/bathymetry) we use the following procedure. For each inundated grid point on land we find the nearest point on the coastline (projection of the inundated grid point onto the coastline) and calculate the distance between the two. Next we divide the coastline into short segments ($\sim$ 10m). We then compare inundation heights and distances to the coastline of the grid points projected into the same segment. Per segment, we take the largest distance as the inundation distance and the maximum inundation height as the runup height.

Tsunami model sensitivity to slip uncertainties

Because tsunami models are computationally expensive, we do not run all models that underly the slip inversion, instead we focus on the optimally fitting model for each scenario. Still, we want to be able to test how uncertainties in the slip solutions affect tsunami model results, and hence how robust our tsunami model results are for each of the fault scenarios. Therefore, for each scenario we draw a number of less likely models from the large distribution of fault slip solutions. We run the tsunami model for a selection of less likely models, which we select based on i) deviations with respect to the mean vertically displaced water volume, or ii) differences compared to the mean vertical displacement field.

5.1 Tsunami inundation distance from satellite imagery

We derive tsunami inundation by classifying pre-post tsunami satellite imagery from the Planet (2018-10-01) and Worldview-3 (2017-11-04; 2018-02-20; 2018-08-17; 2018-10-01; 2018-10-02) archives. For this purpose, we visually compare the pre- and post-tsunami satellite images to manually detect changes that indicate tsunami impact (e.g. coastline changes, debris cover, etc) and digitize the outlines of inundated areas based on this comparison. We take the minimum distance from the inundation outline to the coast to derive the inundation distance. For survey data, we use the reported locations from runup height and inundation height observations (Omira et al. (2019); Putra et al. (2019); Syamsidik et al. (2019); Mikami et al. (2019); Goda et al. (2019); Widiyanto et al. (2019)) and project these on the coastline to compute inundation distances that are consistent with the other calculated inundation distances.

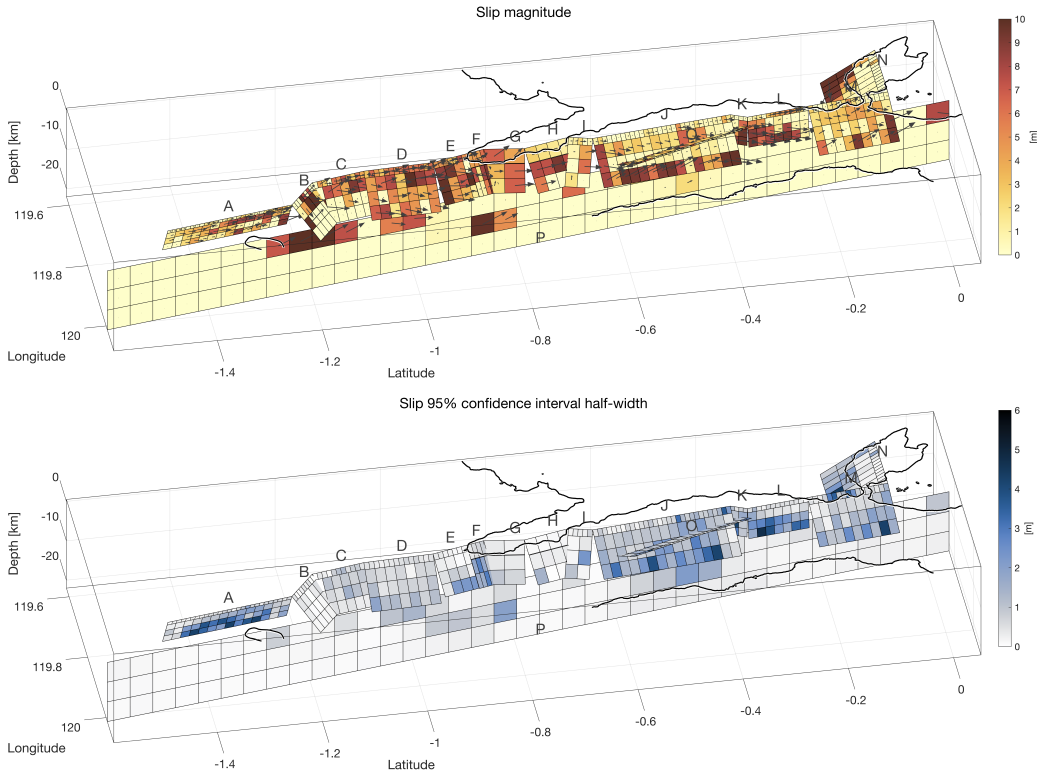

Figure 7. Estimated median fault slip distribution (Scenario IV). (top) Slip magnitude, with arrows indicating slip direction. (bottom) Uncertainties of the slip magnitude, shown as the half-width of the 95% confidence interval, estimated from the slip probability distributions. Bay segments are F,G and H.

6 Finite fault slip estimate

General fault and slip characteristics

The Bayesian slip inversion results in a probability distribution for the estimated fault geometry and slip parameters. Figure 7 shows our median estimate for the fault slip distribution (*Scenario IV*, but results for the different scenarios only differ in the Bay area), demonstrating a dominance of shallow strike-slip, mostly limited to the upper 10 km. On the segments south of the bay, large slip (>5 m) continues up to the surface, whereas segments north of the bay feature no or minor slip on the upper segments, implying that the rupture does not reach the surface there. On the north-south striking segments strike-slip is dominant, but we find significant dip-slip at the fault bend segments. Specifically, we estimate a large normal component (> 1 m) on the releasing fault bend segment B, in southern Palu Valley, clearly connected to the large subsidence observed by GPS and SAR, see figure 3. Furthermore, we find significant dip-slip on the segments below the bay (where we expect a restraining bend), for all tested scenarios. We estimate uncertainties for inverted slip by taking the half-width of the 95% confidence interval of the slip probability density functions (PDF) (of which we show a selection in supplementary figures S9 to S11). Uncertainties in strike-slip and dip-slip components are small in the Palu Valley area, where we have many observations close to the surface rupture. On some other segments the slip is less well constrained; notably on the normal fault segment below the Sulawesi Neck (O), below the Bay (segments F, G, H) and the deeper parts of the Sulawesi Neck segments K and L. Especially on the deeper parts of the normal fault (O), and the deeper part of the southernmost segment the 2σ uncertainties are on the order of the resolved slip. We find short wavelength variability of slip; on the aforementioned segments with high slip uncertainties, we attribute this to the absence of smoothing constraints in the inversion. On the shallow segments though - where uncertainties are generally low - the fluctuation of slip is likely real, as it reflects the spatial variability of co-seismic surface displacement along the fault (see figure 3).

The estimated dip angles show a preference for 40-50 degrees, except below the peninsula (segments K and L) and the deep segment P, see figure 8. Also, there is an approximate continuation from the shallow segments to the vertical deep fault segment. Normal faulting on the parallel segment O reflects the observed subsidence and eastward motions. All scenarios give similar fits to the geodetic data, supplementary figure S13 shows the fits to the SAR displacements fields. The displacements resulting from the median slip distribution well reproduce the GPS displacements, with no significant differences between the scenarios in the Bay area.

Inverted slip below the bay

All scenarios provide a similar fit to the surface displacements. What the scenarios have in common is that the estimated slip below the bay features significant strike-slip, like the remainder of the rupture. Moreover, figure 9 shows that to explain the GPS displacements around the bay, all scenarios require substantial thrusting below the bay. GPS vectors south of the bay (figure 3) point towards the fault, rather than parallel to the mean strike of the fault. We can only explain the azimuth of the GPS displacements by thrusting (dip-slip) on shallow sections of the bay segments of the fault (see supplementary figure S12). In scenarios *I, II* and *IV, V*, we have designated segments as oblique thrust. Those thrust segments become bends in the inversion, by having a strike deviating from the average fault strike. These bay segments also take up the largest part of the thrust slip (even though thrusting is allowed on the left-lateral strike segments), especially in the most shallow parts. In *Scenario III* and *Scenario VI*, where we have not enforced slip to be oblique thrusting on any of the segments, thrusting occurs as well below the bay in those scenarios, but it is more distributed and its magnitude is smaller.

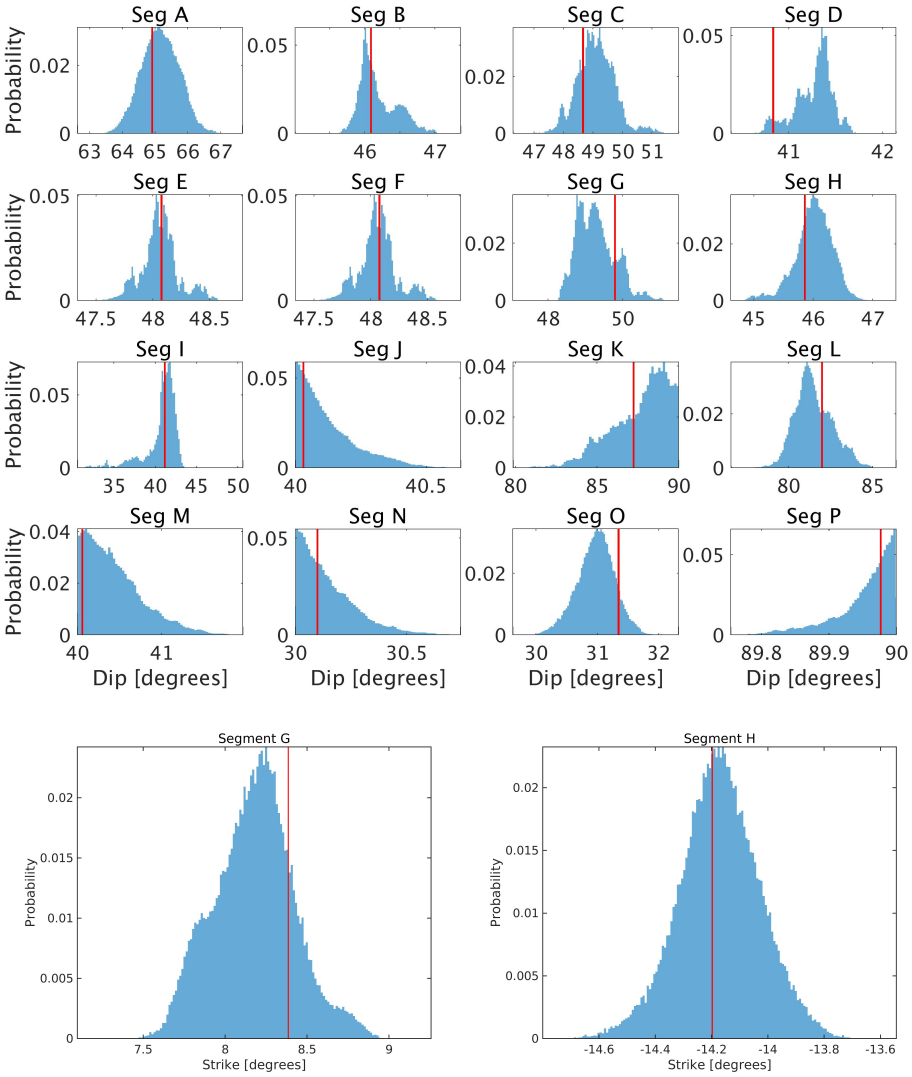

Figure 8. Posterior probability density functions (for *Scenario IV*) of: (top panels) the estimated segment dip angles. All segments dip towards the east, except A and O dip towards the west, and N dips towards the south. (lower row) The strike angles of the central (G) and northern (H) bay segments with a free strike. Red lines denote the value for the MAP (optimal) solution. For locations of the segments, see figure 7.

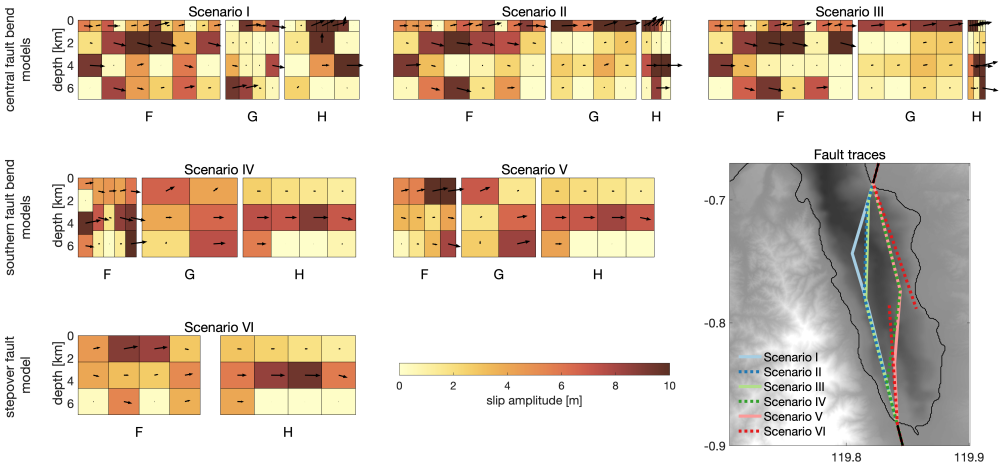

Figure 9. Focus on the inverted slip (MAP) on the fault below Palu Bay for the various fault scenarios. Bay fault segments F, G and H (from south to north) have different rake boundary conditions between the scenarios, see figure 6. The scenarios are grouped as *I, II, III* having a central fault bend, focusing dip-slip in the north (segments G and H); scenarios *IV, V* incorporating a southern fault bend, that allows dip-slip more southerly (segment G), whereas scenario *V* features a step-over (missing segment G). The map shows the various estimated fault traces.

In *Scenario III* the inversion results in thrusting on all bay segments, in *Scenario VI* thrusting occurs mainly on the shallow parts of the southern F segment. In *Scenario VI*, the inversion prefers a strike of the most southern bay segment (F) that does not follow the western coast of the bay (such as in figure 1), but rather strikes to the NNE, likely in order to fit the azimuth of the co-seismic GPS vectors south of the bay. The estimated strikes, of those segments that are allowed to change during the inversion, have uncertainties on the order of a few degrees, see figure 8 for PDFs.

Co-seismic bathymetry changes below the bay

As dip-slip has the most influence on vertical co-seismic displacements, the thrust patterns have a direct effect on vertical displacements below the bay, implying uplift above the thrusting patches. Figure 10 depicts the modeled effective bathymetry change d for all scenarios. Major regions of effective uplift result from thrusting on faults, whereas distributed subsidence occurs above the down-dip end of the thrust slip. The modeled effective bathymetry change d (figure 10) combines the direct vertical displacements and the effect of horizontal displacement on steep slopes (equation 1). Figure S15 in the supplementary material shows the separated contributions from vertical and horizontal co-seismic displacements to the effective bathymetry change. Uplift in scenarios *I, II, III* focuses in the north of the bay, with smaller patches of uplift along the southern F segment. The magnitude of uplift is larger for scenarios where we constrain the segments to be (oblique) thrusting (scenarios *I, II*), with peak values around 5 m. In *Scenario IV* and *V* the uplifted area shifts to the south, above the central fault bend represented by segment G, while peak uplift values are roughly half as those of scenarios *I, II*. The absence of a fault bend in *Scenario VI* leads to smaller uplift values compared to scenarios with a fault bend. The contributions from horizontal displacements of the sloped bathymetry are generally second order effects. Scenarios *I, II, III* predict broad regions of subsidence in the southern part of bay, while subsiding areas in scenarios *IV, V, VI* are smaller. This

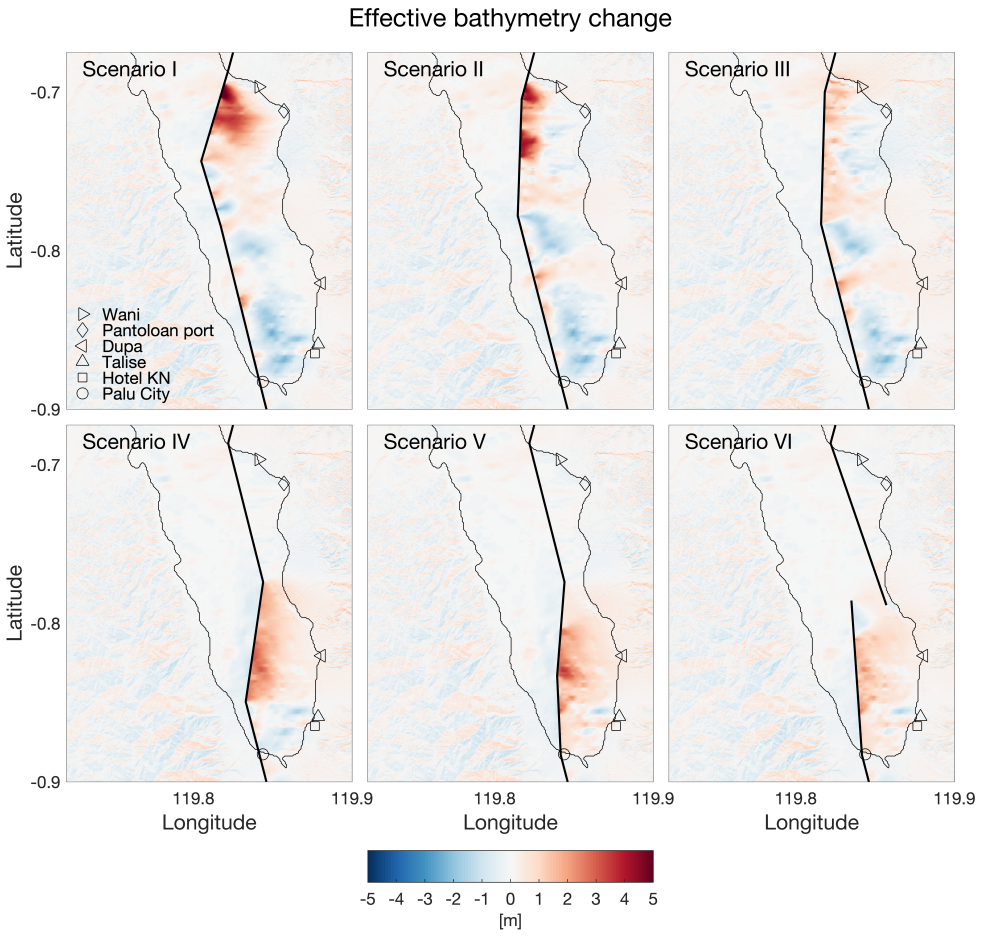

Figure 10. Effective vertical displacements d (eq. 1) below Palu Bay due to co-seismic vertical and horizontal displacements, based on the maximum posterior (MAP) of the 6 fault scenarios. The black line represents the fault trace. Also shown are the six sites for which Carvajal et al. (2019) assembled tsunami elevation waveforms, and that we use in the subsequent section to test the fault scenarios.

subsidence is largely canceled by the effect of horizontal displacements (supplementary figure S15), as the northwards displacement of the sloped bay floor effectively reduces the bathymetry.

7 Tsunami model results and observational constraints

7.1 Tsunami arrival for 6 fault scenarios

Before examining the details of the modeled tsunami evolution, we compare the tsunami waveforms of each scenario to the available tsunami timing observations. We focus primarily on the arrival times of the leading waves of elevation or depression. We typically neglected reflected waves as it is not possible to determine the source region due to the resulting interference. Subsidence is associated with negative polarity of the

leading wave, while uplift is associated with positive polarity. The arrival time, amplitude and polarity of the tsunami waves at the coast provide a first order check of the likeliness of the co-seismic uplift patterns and location. However, the observational constraints on the tsunami evolution are quite sparse. The most reliable sources of information are the waveforms at six locations along the southern and eastern bay coast that Carvajal et al. (2019) derived on the basis of tsunami videos made during and directly after the earthquake. The only tide gauge in the bay, at the harbor of Pantoloan, is likely of little use to observe the tsunami arrival; as data at the tide gauge has been averaged over 30 seconds and output at a 1 minute sampling (Sepúlveda et al., 2020), it cannot be used to describe the short period waves that have been observed from the videos. As our inversion is independent of tsunami timing data, our predictions are unlikely to fit the video tsunami waveforms exactly. Rather we judge the models for a qualitative agreement with the available data.

Figure 11 shows the model evolution of the relative tsunami elevation (equation 2) for the first 6 minutes after the earthquake, compared to the video waveforms deduced by Carvajal et al. (2019).

Northeastern sites: Pantoloan and Wani

At Pantoloan the largest, and presumably first, waves have been relatively well observed by the motion of a ship in the dock by a camera. The video waveform shows a first major, negative wave at around 3 minutes since the start of ground shaking, followed by a 2.5 m wave of elevation less than 30 seconds later. We observe that all scenarios with a northern fault bend, scenarios *I, II, III*, lead to an arrival of a major positive wave between 1 and 2 minutes, well before the first observed wave. Scenario *III* leads to reduced amplitudes of the first waves compared to *Scenario I* and *II*. For Wani, similar as for Pantoloan, scenarios *I, II, III* predict an early wave arrival (1 min) before the onset of flooding as observed. Scenarios with a southern fault bend *IV, V, VI* produce a first, positive wave arriving 3 minutes, but underestimate the wave amplitude by approximately a factor of two.

Southeastern sites: Dupa, Talise and Hotel KN

The video waveforms for Talise and Hotel KN are based on videos that record the earthquake induced shaking, and have thus a reliable timing. For Talise it is merely the drawdown of water that is captured on the video, within a minute from the start of the shaking. We model a fast ($<$ 1 minute) approach of a wave of depression near Talise and Hotel KN (see the supplemental videos). For scenarios *I, II, III* the wave of depression has the largest amplitude, while in scenarios *V, VI* this negative wave just misses Talise due to interference with a wave of elevation. The subsequent inundation by waves of elevation is not visible from the Talise video, but it is recorded from cameras at Hotel KN, just south of Talise. All scenarios predict a negative wave at approximately 1 minute for Hotel KN (the videos at this location do not provide information on the first 1:40 minutes), quickly followed by the arrival of a positive wave. Scenarios *IV, V, VI* predict this arrival 20 seconds earlier than the video waveform, scenarios *I, II, III* lead to a 20 seconds later arrival compared to the video waveform. Amplitudes between video waveform and models are very similar.

At Dupa, north of the two former locations, the earthquake itself is not recorded by camera, resulting in a time bias. In the video it takes 1:50 before the arrival of the positive wave (Carvajal et al., 2019), while a tsunami bore can be seen close to the coast 30 seconds prior to arrival. Assuming that the duration of the strongest earthquake shaking is about 30 seconds (as is visible in the video from nearby Talise), the arrival of the

positive wave can be at the earliest at 2:20 since the start of the earthquake, which is 30 seconds earlier than suggested by Carvajal et al. (2019). Scenarios *I, II, III* all feature a first negative wave, and small (< 1 m) positive waves after 2:30 minutes. Scenarios *IV, V, VI* do not lead to initial negative waves (due to absence of subsidence near Dupa), and predict the first major positive waves at 1:50 minutes.

Palu City

Whereas the nearby locations Hotel KN and Talise have very early arrival times of the first positive waves, Carvajal et al. (2019) suggest that the first, and positive, wave arrives at Palu after 3 minutes, while there is a time bias, as all videos from Palu start after the earthquake. Sepúlveda et al. (2020) suggest that for Palu City the time bias uncertainty is 30 seconds. Even though the rupture went through Palu City, waves are likely to arrive relatively late due to the shallow bathymetry offshore Palu. All scenarios predict an initial drawdown of water at the Palu coast (< 1 m), and positive waves arriving after 3 minutes. In *Scenario IV*, the timing of the first wave arrival at about three minutes corresponds to the video waveform, while the other scenarios predict a first arrival after 4-5 minutes. Except for *Scenario VI*, the crest amplitude is comparable to that of the video waveform, yet none of the models reproduce the negative wave that follows the first positive wave around 4 to 5 minutes after the earthquake.

7.2 Preferred fault scenario: southern located fault bend

In selecting a scenario that best explains the observed tsunami waveforms, we prefer scenarios that best explain arrival time and initial polarity and amplitude, while we disqualify scenarios that include significant initial waves that did not occur according to the available observations. As all our model scenarios with a northern fault bend (scenarios *I, II, III*) lead to a tsunami arrival that is too early in northeastern sites Pantoloan and Wani, we discard these scenarios. In scenarios *IV, V, VI* the areas of major uplift localize in the south, which avoids a tsunami that arrives too early in Pantoloan and Wani. As *Scenario VI* underestimates the wave amplitude in Palu City, because it lacks a fault bend, we discard this scenario also. We choose *Scenario IV* as a preferred fault scenario, since it explains wave amplitudes and polarity for the other sites (Dupa, Talise, Hotel KN and Palu City) and does a relatively good job in predicting the timing of the first arrivals, even though this scenario lacks significant waves in the northeast. *Scenario V* is comparable to *Scenario IV*, but as the latter has a more prominent southern corner at the fault bend (figure 10) it has more pronounced waves travelling directly towards Palu, which improves the arrival time fit. In the remainder of the paper we show results for scenario *IV*, and include the other scenarios in the supplementary section 8.

Spatiotemporal evolution of the initial tsunami waves

Our preferred scenario *IV* predicts the propagation of two approximate north-south wave fronts in the direction of both the western and eastern bay coastlines, see figure 12. At 1:40 after the earthquake, the model predicts reflections at the western coast that take the form of localized elevation perturbations (between latitudes -0.85 and -0.8), which result in subsequent ringing (see supplemental video S1). At the east coast the positive polarity waves arrive shortly after 1:40. The panels show also the relatively slow approach of several tsunami fronts towards western Palu, which approach Palu from different directions (3:20 and 4:10) due to the local shallow bathymetry. In this scenario the waves radiating towards the north have only moderate amplitudes compared to the waves traveling in the N-E and southern directions.

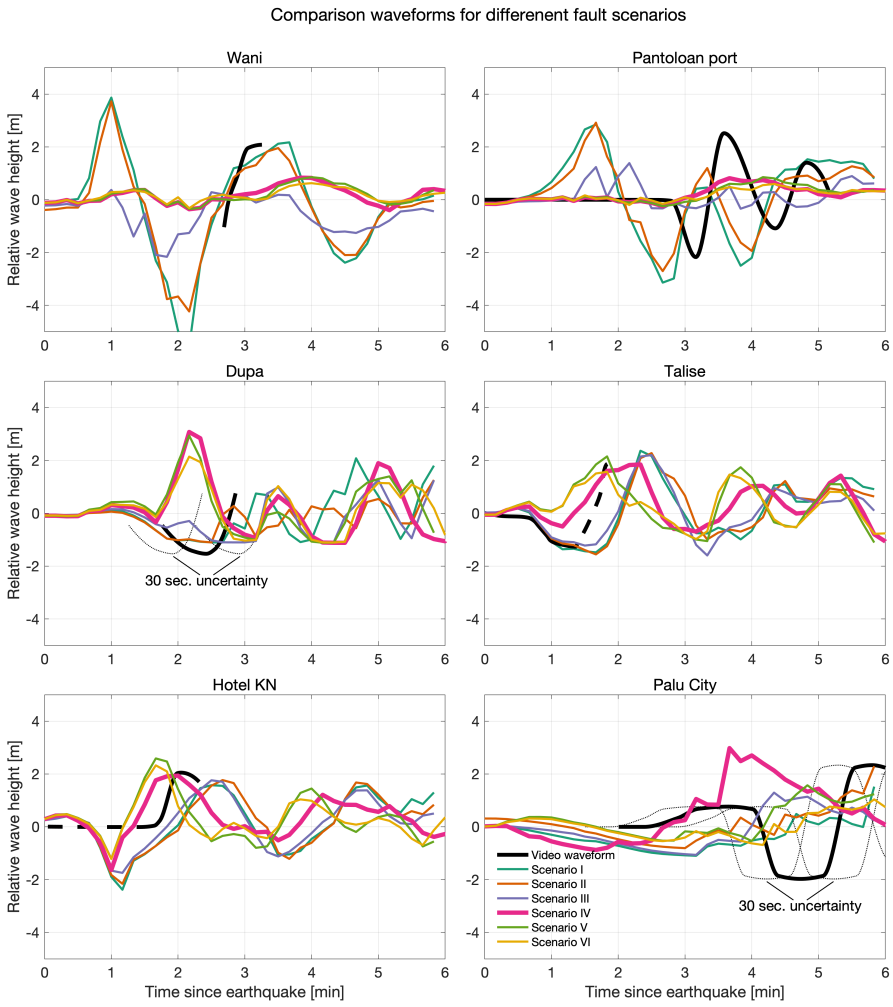

Figure 11. Approximate tsunami height at six locations for which tsunami observations are available, based on video analysis from Carvajal et al. (2019), and model predictions for tsunami height. For locations see figure 10. Time series for Dupa and Palu City have a bias in timing as the start of the videos does not include the earthquake (Sepúlveda et al., 2020). *Scenario IV* represents our preferred solution. A dashed line represents a lower confidence estimate (Carvajal et al., 2019).

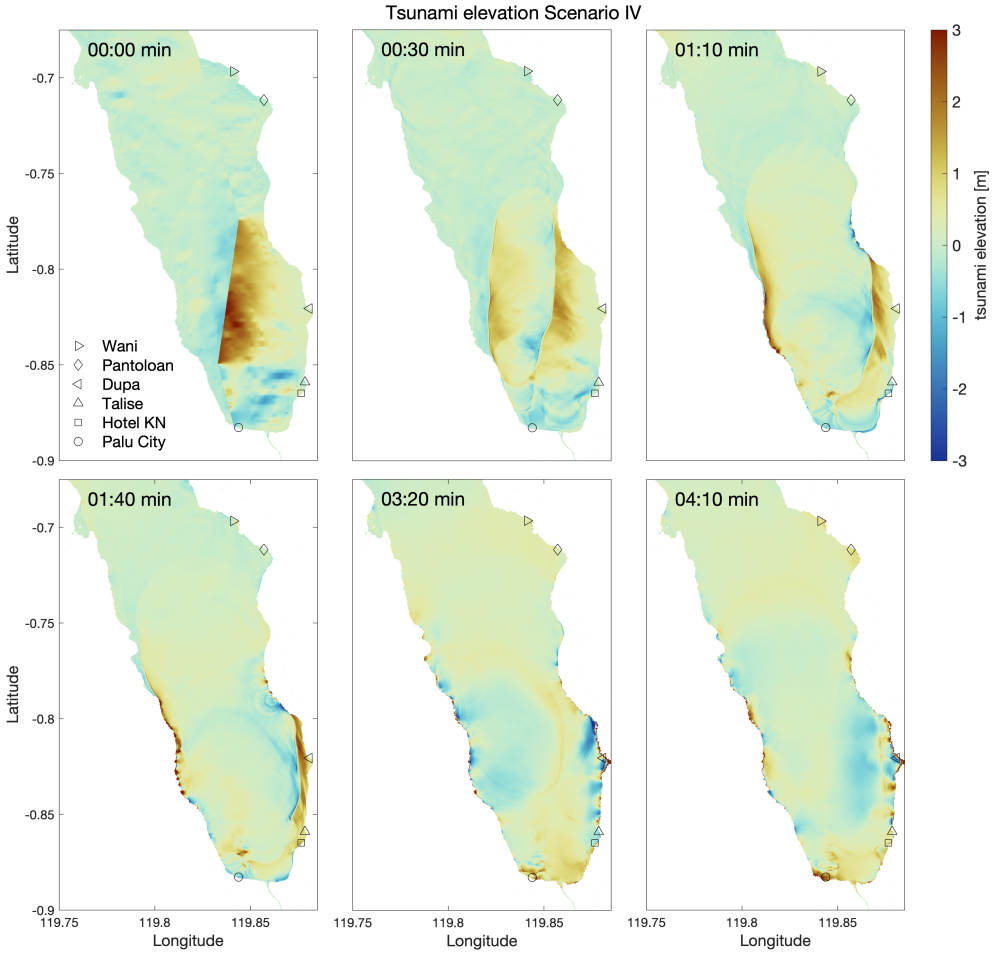

Figure 12. The evolution of the tsunami elevation (w.r.t. tide at the earthquake time) of scenario *IV* at 6 different epochs. The continuous evolution of the tsunami elevation can be found in supplemental video S1.

7.3 Comparison to survey runup data

We compare modeled runup to observations from field surveys and optically derived runup distances in figure 13. This figure shows runup and inundation height as a function of distance along the coast, subdivided in the western, southern (Palu City) and eastern coast. To improve visibility of the optically derived inundation distance, we apply a moving median filter of 250 m length, and show the 1-99 percentiles within this window as a measure of variability. In general terms our model produces comparable runup heights as reported from surveys, with maximum values around 8 m (around Watusampu at the west coast of the bay). Only around Wani and Pantoloan do we systematically underestimate the runup heights. The runup comparison also strongly favors models with a fault bend in the southern part of the bay, as scenarios *I, II, III* consistently overestimate runup in the north of the bay and underestimate runup heights along the southern bay coast (see supplemental figure S16).

Inundation distances derived from satellite imagery agree well with inundation distances that we compute from surveyed locations. We model inundation distances in western Palu City that are comparable to those observed, but underestimate inundation distance at many other locations. We do not use reported flow depths because the DTM is at many places not representative for the coastal topography due to inclusion of vegetation and buildings.

Robustness of the preferred scenario

Using the preferred *Scenario IV*, the uncertainties in the slip distribution have only a modest effect on the tsunami evolution, as supplemental figure S19 shows that the MAP solution and the selection of extreme models have nearly identical tsunami model results. The timing, amplitude and polarity of the tsunami elevation is very similar compared to the maximum posterior model (MAP), suggesting that under certain fault boundary conditions (i.e. the fault scenarios) the tsunami evolution is not very sensitive to uncertainties in slip distribution.

8 Discussion

The 28 September 2018 M_w 7.5 Palu, (predominantly) strike-slip earthquake unexpectedly generated a tsunami in Palu Bay. In this study, we integrate a large set of geodetic data to determine a high-resolution 3D surface deformation field, invert for subsurface slip distributions for several plausible (offshore) finite fault scenarios, and compare consequent tsunami models with available observations. The subsequent sections consider the strengths and limitations of our approach and the available data, and our interpretation of these data compared to previous studies. Finally, we broaden the implications of transtensional and transpressional tectonics to the tsunamigenesis of strike-slip faults.

8.1 Resolving co-seismic displacements

Fault trace

Our combination of co-seismic GPS and SAR data provides a view on the surface displacements that is complimentary to earlier reports, but also uncovers previously unknown aspects. The north-south displacements, typical for a left-lateral strike-slip fault (figure 3 or supplemental figure S4 for the north component only), confirm earlier reports of a offsets of a few meter on surface ruptures in Palu Valley, based on optical data (Sotiris et al., 2018; Socquet et al., 2019; Jamelot et al., 2019; He et al., 2019; Bacques et al., 2020). In our analysis the surface rupture is best resolved using the SAR azimuth offsets and MAI (see supplemental figures S13 to S13). In the Sulawesi Neck we find no clear indi-

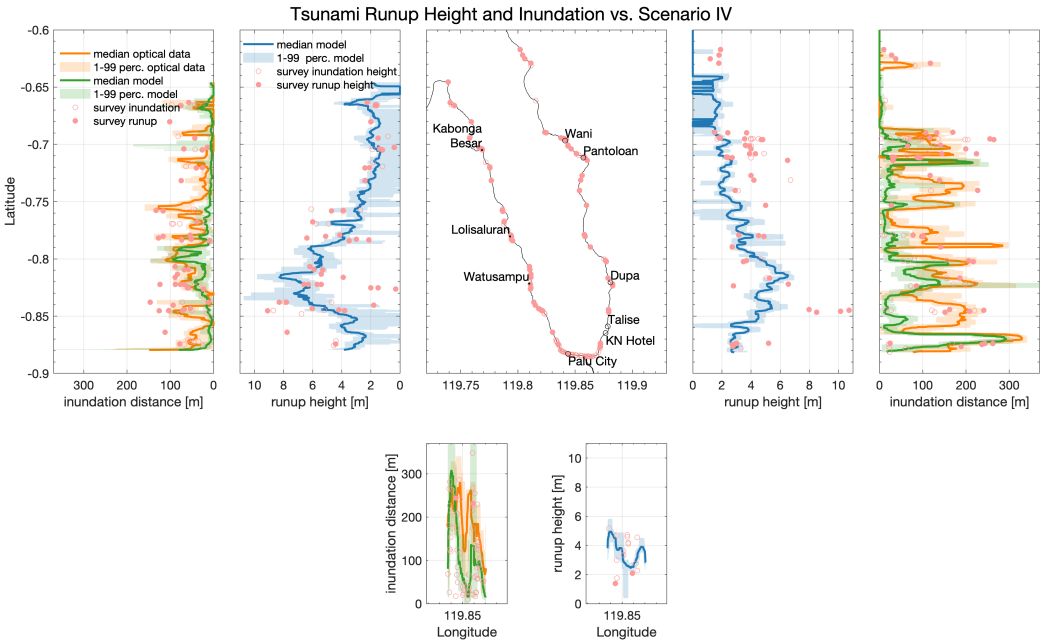

Figure 13. Comparison of observed runup height and inundation distance with results from the preferred *Scenario IV*. The middle panel shows the surveyed locations. The two left panels show modeled and observed the inundation distances, and the runup height at the west bay coast, respectively. The two right panels show the runup height and inundation distances for the east coast, respectively. The two lower panels show the same quantities for the southern bay coast, around Palu City. The inundation height and distances should be regarded as minimum values for that particular site. Surveyed runup heights and inundation distances are taken from Omira et al. (2019); Putra et al. (2019); Syamsidik et al. (2019); Mikami et al. (2019); Goda et al. (2019); Widiyanto et al. (2019). We apply a moving median filter to our optically derived inundation distance and to the modeled quantities (as a function of location at the coast), with a moving window of 250 m, and show the 1-99 percentile within this moving window.

cation of a sharp surface rupture, which may either indicate that slip did not reach the surface or that the displacement occurred in a more distributed sense by off-fault deformation. We do find strong indications of normal faulting, parallel to the main fault in the Sulawesi Neck that has not been reported previously. All GPS and SAR observations have been acquired within a few weeks after the earthquake: 1 to 42 days for a few GPS sites, and within 4 to 27 days for the SAR data. Nijholt et al. (2021) report post-seismic displacements on the order of a few cm in the first year since the event, which is two orders of magnitude smaller than the largest co-seismic estimates. So, while our observations are not purely co-seismic we expect relatively small contamination from post-seismic relaxation. Still, the estimated normal faulting in the Sulawesi Neck is mostly based on SAR-displacement fields based on data 18 to 27 days after the actual earthquake, and the weighted root mean square misfit peaks around the inferred normal fault (see supplemental figure S8). Hence, we cannot rule out that the activity observed off the main fault in the Sulawesi Neck has been an ongoing process unfolding during the observational period.

Tectonic setting

The tectonic setting of the Palu Bay and Valley conforms to a transtensional basin: a main subsurface fault underlying the sedimentary basin(s) splays upward into distinct, small-scale fault strands in a negative flower structure (see figure 5). The orientation of Riedel shear structures, which are commonly attributed to strike-slip faults (figure 4), and the azimuth of interseismic velocities (Socquet et al., 2006) support that the main subsurface fault runs approximately parallel to the inferred fault traces at the Sulawesi Neck. Such an azimuth is in accordance with e.g., Walpersdorf, Vigny, et al. (1998), and our deep fault orientation is different from the previously assumed offshore continuation. Namely, many studies assumed that the main fault trace along the west side of Palu Valley continued approximately along the west side of Palu Bay (Bellier et al., 2001, 2006; Natawidjaja et al., 2020). We concur with Stevens et al. (1999) that the deep, main fault trace is likely east of Palu Bay. While the overall setting is transtensional (figure 5), we observe multiple onshore fault bends, both releasing bends leading to slip with a large normal component, as well as restraining bends that involve thrusting (figure 7).

GPS displacement azimuth variation

We find that the azimuths of the co-seismic displacements are mostly parallel to the average strike (350°). However, south of the bay, around Palu City, GPS co-seismic displacement vectors point consistently more to the west than elsewhere at comparable distances to the fault. These details in the displacement field are important for the interpretation of slip and fault geometry below the bay, where no direct observation of the surface displacement is possible. He et al. (2019) estimate a co-seismic 3D displacement field based on azimuth and range offsets from ALOS-2, from one ascending and one descending orbit and optical data from Sentinel-2. While they observe a similar displacement field as we present, their noise levels are larger, as SAR offsets and optical data have a lower precision than our dataset. Therefore, the addition of GPS data is important to detect the deviating co-seismic displacement azimuth south of the bay.

Vertical displacements

The vertical co-seismic displacement along the fault is generally minor; on the order of a few 10s of cm, see figure 3. Only along fault bends, do we observe significant subsidence or uplift. Notably, along the southern releasing bend we observe up to 1.8 meter subsidence (indicated in figure 3 by *d*), which is well constrained by GPS site *PNDE*. Previously, there were no good constraints on the vertical co-seismic displacements, even though the lower signal-to-noise vertical displacement estimate from He et al. (2019) al-

ready hinted at significant subsidence north of the southern, releasing, fault bend in Palu Valley. While smaller in magnitude, we observe notable uplift north of two restraining fault bends in the Sulawesi Neck, indicated by *e* in figure 3.

Our study benefits from the combination of SAR and GPS data, and lacks the spurious displacements that are often found in the far-field results from optical data or SAR offset data. The large dataset also allows us to observe secondary features, such as the subsidence and westward motion in the Sulawesi Neck, east of the main fault.

8.2 Inferred slip distribution

Shallowness of rupture

The 2018 Sulawesi earthquake can be described as a generally shallow event; especially in Palu Valley, our slip inversion indicates that peak slip (up to 10 m) occurred in the upper 7 km with significant slip right up to the surface. While localized slip does not seem to have reached the surface in the Sulawesi Neck, slip prevails in the upper 7 km. Only at a few isolated locations does our inversion put relatively large (> 5 m) slip below 7 km on the deeper, straight fault segment. This is a similar picture as in Socquet et al. (2019); Williamson et al. (2020); He et al. (2019); Bacques et al. (2020), where the latter two studies also find a lack of very shallow slip below the Sulawesi Neck. In our model there is considerable variation in the amount of strike-slip in the shallow portions of the fault in Palu Valley, which we relate to the variability in fault-parallel and fault-perpendicular displacements, see figure 3 or supplemental figure S4 for separate eastwards and northwards displacement. Seismology-based finite fault solutions lack the sensitivity to constrain the segmented geometry of the fault, and fault bends in particular, and thus have limited power for understanding tectonic causes of the subsequent tsunami. While seismological inversions recover a large slip asperity in the southern portion of the rupture, some studies place the large slip area too far north, in the bay rather than in Palu Valley (USGS, 2018; Yolsal-Çevikbilen & Taymaz, 2019). As Lee et al. (2019) show, seismological slip solutions can be more in agreement with geodesy around the location of the large slip in the southern part of the rupture when allowing higher rupture velocities. Generally, slip models based on seismological data confirm that the peak slip during the event was shallow (<10 km) (Fang et al., 2019; Zhang et al., 2019; Li et al., 2020). The shallow depths of the rupture agree well with the interseismic locking in the upper 12 km only, as inferred from GPS data (Socquet et al., 2006).

Sensitivity of the geodetic data to sub-bay slip

Whereas co-seismic uplift from thrusting below the bay cannot be observed directly, we infer thrusting on a restraining fault bend below the bay, connecting the clearly observable north and south onshore fault strands, to explain GPS and SAR displacements (figure 9). Thrusting below the bay has been proposed before by Socquet et al. (2019) and He et al. (2019), but most previous fault slip solutions for the Palu earthquake have been hampered by lack of constraints on vertical deformation, or have relied on north-south displacements only. In our various fault scenarios, the thrusting on fault bends is largest when we allow thrusting to become larger than the left-lateral strike-slip component (i.e. scenarios *I, II, IV, V*). As figure 10 shows, uplift of more than 2 m concentrates above the fault bend segments in these scenarios. In other fault models, such large dip-slip, and accompanying uplift, is either lacking (Y. Wang et al., 2019; Williamson et al., 2020; Bacques et al., 2020) or has a smaller magnitude (Socquet et al., 2019; He et al., 2019; Jamelot et al., 2019; Sepúlveda et al., 2020).

Our estimated dip angle of the thrust segments is also considerably smaller than the large dip angles in other studies: $70-90°$ (Sepúlveda et al., 2020); $60°$ (Socquet et al., 2019); $65°$ (Ulrich et al., 2019); $70°$ (He et al., 2019). The subdivision of our fault

model into a shallow and deep part allows a gentler dip angle in the shallow parts, and a steep dip for the deep fault. The dip-angle has a large influence on balance between the estimated uplift and subsidence below the bay. Large, near-vertical, dip angles lead to comparable uplift and subsidence magnitudes (Ulrich et al., 2019; Bacques et al., 2020), while our models (figure 8) clearly prefer shallow dip angles of around 45-50°. Comparable dips are only found in Jamelot et al. (2019), who find a preference for a 45° dip angle for the fault bend - in a setup similar to Scenario *I* - which leads to predominant uplift and only minor subsidence above the deeper parts of the rupture. Only the onshore fault segments in the north of the Sulawesi Neck (K,L) favor contrastingly large dip angles (comparable to the USGS moment tensor solution with a 66° dip (USGS, 2018)). We find a single case of westward dip, in the southernmost part of the rupture. On the other hand all fault bends (also those onshore) clearly favor much shallower dips (figure 8).

We also resolve considerable thrusting in a scenario without explicit thrust constraints on the sub-bay fault bend (*Scenario III*), yet it is more distributed (figure 9). In the scenario without a fault bend, but rather a step-over (*Scenario VI*), the inversion leads to thrusting on the southern bay segment. In this case there is a distinct strike change compared to the fault onshore, in order to explain the nearby GPS displacements. The fit to the GPS displacements and SAR data in the vicinity of the fault, is comparable for all scenarios.

Secondary faults

The eastward and subsiding motion east of the fault in the Sulawesi Neck, around latitude 0.5°S, can be explained by normal faulting, parallel to the main strike-slip rupture. Following Socquet et al. (2019), we partly explain the eastward and subsiding displacements in the Balaesang Peninsula - observed by InSAR and SAR range offsets from pair 3 (figure supplementary figure S13) - by normal faulting on a southward dipping fault. This fault possibly connects the fault on the Sulawesi Neck to the presumed northward continuation of the Palu-Koro fault offshore. Alternatively, He et al. (2019) explain the displacements in the Balaesang Peninsula by a fully offshore fault, running approximately parallel to the onshore main fault. Because of the lack of a clear fault trace, and as most of the apparent fault is offshore, no definite statement about the source of the co-seismic displacement on the peninsula can be made.

8.3 Tsunami potential of the co-seismic displacements

On the basis of the fault model by Socquet et al. (2019), Carvajal et al. (2019) argue that a tsunami driven by deformation due to fault slip cannot match the observed tsunami amplitude. Similar arguments have been put forward by Heidarzadeh et al. (2019) and Jamelot et al. (2019) regarding insufficient model runup compared to observed runup heights by post-tsunami surveys. A number of studies propose landslides as the (partial) source for the tsunami (Takagi et al., 2019; Gusman et al., 2019; Pakoksung et al., 2019; Sepúlveda et al., 2020; Williamson et al., 2020; Nakata et al., 2020). Schambach et al. (2020) model tectonic (using models from Socquet et al. (2019); Jamelot et al. (2019); Ulrich et al. (2019)) and landslide tsunami sources, where the latter are based on pre- and post-earthquake bathymetry analyses of Liu et al. (2020). We argue that the proposed landslide dominance of the tsunami is tentative, mostly due to the fact that previous finite fault slip models have underestimated the uplift due to dip-slip below the bay. Furthermore, most landslide sources are rather speculative, and the timing of the landslide sources is unconstrained. Liu et al. (2020) study bathymetry changes between pre-earthquake surveys from 2014, 2015 and 2017 and post-earthquake surveys conducted in October and November 2018. Differences between the 2014 or 2015 bathymetry and the post-earthquake bathymetry reveal bathymetry changes (> 50 m) that are much larger than the changes at presumed submarine landslide locations, and results from 2014 are

not consistent with those from 2015. On the other hand, the 2017 survey only covers a small part of the northern bay (close to Pantoloan), but differences with the post-earthquake survey are much more localized, providing reasonable indications for at least two submarine landslides close to Wani and Pantoloan.

Southeastern coast

While we do not rule out contributions from landslides, or more specifically, submarine landslides, our models show that displacements due to co-seismic slip are most likely the major tsunami source. This applies especially to the stretch of coast between Palu City northeastwards to Dupa, where timing constraints on the first tsunami arrival are available. An interesting feature of the video analysis of Carvajal et al. (2019) is the early (1-2 min) arrival of the first tsunami waves in the southeast coast of the bay (Hotel KN, Talise and Dupa) compared to more northern sites at the eastern coast (Pantoloan, Wani) (3 min) suggesting a source within the southern part of the Bay. Takagi et al. (2019) proposed (submarine) landslide sources at the western bay coast, but modeled arrival times for the southeastern coast at the video waveform locations are 1 to 2 minutes too late. Similar results can be found in Liu et al. (2020) and Schambach et al. (2020), where landslide-only tsunami models cannot explain arrival times in the southeastern bay coast. Alternatively, all our models reproduce the arrival times and polarity in this area (Hotel KN, Talise and Dupa, figure 11), even though our arrival times may be off by 30 seconds. This leaves open slight deviations in exact uplift locations, but requires a location within the bay, rather than submarine landslides at the western bay coast.

Western coast

Our preferred *Scenario IV* can explain all observed runup heights at the west coast, except that we predict the runup height peak of 8-9 m at Watusampu to occur slightly farther north than what has been observed (figure 13). Scenarios with a northern fault bend, e.g. *I, II, III*, unanimously overestimate the runup in the northern parts of the bay (see supplemental figure S16), which is an additional clue that the uplift should be located more to the south, such as in our preferred scenario *IV*. Our preferred fault scenario predicts very early arrival of the tsunami waves at the west coast, at around 1:30 minutes, see figure 12. The features that look like rings of sea surface elevation at the western bay coast as photographed from an airplane 1:50 minutes after the event have been interpreted as landslide sources Carvajal et al. (2019), but our model also produces similar features after the first waves hit the coast and reflect after 1:40 minutes (figure 12, and supplemental video S1).

Palu City

The relatively late tsunami arrival (5-6 min) at Palu can be explained by the shallow bathymetry (as also noted by Takagi et al. (2019)) offshore western Palu. The fault scenario with a clear fault bend (our preferred *Scenario IV*) leads to the best arrival time, and most of our models can reproduce the up to 5 m of runup height here (figure 13, and supplemental figure S16 for the other scenarios). The model suggests a complex wave arrival pattern, with multiple waves traveling both from the northeast as well as the northwest, a characteristic that Carvajal et al. (2019) also observe from their video analysis.

Wani and Pantoloan

Since the geodetic co-seismic observations allow for various fault geometries below the bay, additional data are required to constrain the fault geometry setup. While arrival times of the first tsunami wave in the southeastern part of the bay are relatively

insensitive to the fault geometry, the arrival time at Pantoloan (and to a minor degree Wani) puts a tighter constraint on the tsunami source. Models with uplift above the northern sub-bay segment of the fault, scenarios *I, II, III*, always lead to an overly early arrival at Pantoloan. Previously, results from Ulrich et al. (2019); Jamelot et al. (2019); Williamson et al. (2020); Schambach et al. (2020) illustrate the difficulty to explain the Pantoloan tsunami arrival times when the co-seismic source is close to the location where the rupture entered the bay. As an exception, Gusman et al. (2019) propose a co-seismic vertical displacement field that places Pantoloan exactly at the hinge line that divides an area of uplift from a subsiding area, but it is difficult to relate this long-wavelength displacement field to a tectonic source. Late tsunami arrival in Pantoloan naturally places the fault bend more southerly in the bay. In scenarios *IV, V, VI* we used the 170 s travel time contour of Carvajal et al. (2019) to locate areas of significant vertical displacements. Such a southern fault bend location, however, does not explain 2 m waves observed at Pantoloan and Wani, since largest waves travel perpendicularly to the fault bend (roughly east-west), rather than towards the north. Also the observed negative polarity of the first arrival at Pantoloan poses a problem, as all our model scenarios predict a positive wave travelling to all coasts, because of the predominance of uplift compared to subsidence (similar to models from Sepúlveda et al. (2020); Williamson et al. (2020); Schambach et al. (2020)).

Tsunami potential of co-seismic displacement

From the range of tested fault scenarios below the bay, we can confidently state that at least the tsunami observed in the southern part of the bay is directly related to the earthquake rupture. The arrival time in this section can best be explained with a source located in the deeper parts of southern bay, where we predict up to 2 m uplift in our preferred scenario. All tested scenarios that explain the geodetic observations lead to runup heights that are of the same order as what has been observed by post-earthquake surveys (see figure 13 and supplementary figure S16 for the remaining scenarios). While the available tsunami timing data are sparse, the runup and inundations heights have been well sampled along the bay. Bathymetric surveys put minimal constraints on possible landslide sources along the western and southern coast, and while we do not rule out such sources of tsunami waves, landslides are not needed to explain the general arrival time and polarity of the leading waves, and observed runup along most of the bay coast.

Contrastingly, we have not been able to find fault geometries that can explain the relatively late arrival of tsunami waves at Pantoloan and Wani, even though these sites are quite close to the location where the rupture has entered the bay from the Sulawesi Neck. This leaves the option open for other sources, such as tsunami waves generated by landslides, especially sites close to Pantoloan, as advocated by Liu et al. (2020) and Schambach et al. (2020). From the bathymetric study by Liu et al. (2020) there are indications for such landslides, and assuming a 75 s delay compared to the rupture time Schambach et al. (2020) find a good agreement with the video waveforms at Wani and Pantoloan based on landslide sources only. On the other hand, based on the same landslide sources, Liu et al. (2020) have difficulty in explaining the arrival of the second, positive waves in Wani and Pantoloan, which suggests a significant sensitivity to the exact parametrization of the landslide sources.

Seismological studies report that the Palu earthquake rupture propagated at speeds higher than the shear wave velocity, also known as a supershear rupture (Bao et al., 2019; Li et al., 2020; Ulrich et al., 2019). Coupled rupture and tsunami models show that tsunami wave timing and magnitude is relatively insensitive to rupture speed (sub-shear or supershear speed) when the static fault slip is similar (Elbanna et al., 2021). Furthermore, the long waveperiod (~ 0.5 min) and largest amplitude waves are still generated by the permanent co-seismic deformation, just as for earthquakes rupturing at sub-shear speeds (Ohmachi et al., 2001; Maeda & Furumura, 2013). As our geodetic observations actu-

ally constrain the offshore permanent co-seismic displacements, we already capture the relevant features of the tectonically induced tsunami waves.

As the only available topography data are based on a digital terrain model, that includes vegetation, our model has difficulties explaining the inundation distances such as observed by post-tsunami surveys, as our onshore topography is biased. Tests with lower friction values of the sea bed (for a definition see section 5) do not lead to significant different inundation distances. We are not aware of any other study to the Palu tsunami that compares modeled with observed inundation distances.

8.4 Relevance for other transtensional basins

In recent years, an increasing number of tsunamis have been related to (the direct consequences of co-seismic) strike-slip events, i.e., offshore the Philippines (Imamura et al., 1995), offshore Canada (Rabinovich et al., 2008), within the Sea of Marmara (Altınok & Ersoy, 2000), near and along Haiti (Hornbach et al., 2010; Poupardin et al., 2020), at the San Andreas fault (Geist & Zoback, 1999), in New Zealand (King, 2015), at Wharton Basin (Gusman et al., 2017) and within the Dead Sea (Frucht et al., 2019). This includes settings where strike-slip earthquakes caused tsunamigenic aftershock activity on nearby fault systems (Geist & Parsons, 2005; ten Brink et al., 2020). Notably, strike-slip faults can constitute multiple fault segments at shallow levels, especially in the case of transtensional basins. This thus means that an earthquake rupture in such settings is likely to create localized, vertical, submarine motions able to generate significant tsunamis (Geist & Zoback, 1999; Cormier et al., 2006).

We recognize that the transtensional tectonic setting of Palu Bay (figure 5) is very similar to the well-studied Sea of Marmara and Gulf of Izmit regions of the North Anatolian fault, in that multiple fault strands run across and below the basins in a negative flower setting (Aksu et al., 2000; Yalçıner et al., 2002; Laigle et al., 2008). The difference with Palu Bay is that many tsunamis have been identified and attributed to extensive tectonic activity in the Marmara Sea region (e.g. Yalçıner et al. (2002); Altınok et al. (2011). For example, a multitude of dated submarine mass movements in the Marmara Sea correlate well with documented historical earthquake ruptures (e.g., Drab et al. (2012); Çağatay et al. (2012); McHugh, Braudy, et al. (2014). Importantly, we argue that this does not exclude co-seismic, vertical surface motions as a potential tsunamigenic source. However, in their extensive catalogue, Altınok et al. (2011) only ascribe a limited amount of reported tsunamis to finite fault ruptures. Studies using tsunami modeling in the Marmara Sea point towards a larger potential of (local) destructive tsunami run-up due to (submarine) landslides compared to co-seismic fault ruptures (Hébert et al., 2005; Latcharote et al., 2016). However, these studies include very crude (generic) slip distributions on simple fault geometries. Tinti et al. (2006), on the other hand, conclude that the tsunamigenic potential in the Gulf of Izmit reasonably matches tsunami observations across the shoreline for co-seismic ruptures that include a fault bend zone: smaller scale faults with dip-slip motion in between (longer) segments that host dominant strike-slip motion. The importance of submarine bends, or step-overs, in a strike-slip fault zone thus rivals that of (submarine) landslides. Landslide contributions may then be expressed as local (secondary) features in the tsunami observations (e.g., Tinti et al. (2006)).

Fault bends can also act as impeding features for earthquake ruptures and fault segments active on a geological time scale are not necessarily activated every single time an earthquake rupture front approaches them (Biasi & Wesnousky, 2016). For example, the Hershek restrictive bend connects two main segments of the North Anatolian northern fault strand in the Sea of Marmara and the Gulf of Izmit. The notion of a continuous surface-breaking rupture during the 1999 Izmit earthquake is debated, and the subsidence history over the past two millennia indicates that not every major, tsunamigenic

earthquake that affected this bend resulted in surface-breaking differential motion across the fault interface (e.g., Özaksoy et al. (2010); Bertrand et al. (2011); Lettis et al. (2002)). Fault bend activity, or vertical motion due to geometrical steps, is highly dependent on the activity on its adjacent segments. Besides the potential dip-slip motion at fault bends, other limbs of the negative flower structure can also host significant, oblique motion. Analysis of sediments along basin-bounding faults at the Sea of Marmara reveals co-seismic vertical offsets of up to 1.8 m (Beck et al., 2015). Such offsets are more than enough reason to consider the dip-slip component of any segment in a transtensional basin; distinct jumps in relative vertical motions are not just limited to fault bends or step-overs. An example of this is the overall subsidence in Palu Valley caused by dip-slip on main fault strands (figures 3 and 7).

A strike-slip earthquake is likely to include a rupture across several fault segments, especially when occurring in a transtensional basin. Previously, activity on several fault strands has often been argued to be insufficient to explain observed inundation and runup of tsunamis completely (Öztürk et al., 2000; Cormier et al., 2006), hence the requirement of a secondary tsunami source. There are abundant relations between earthquakes and (induced) submarine mass movements (e.g., Yalçıner et al. (2002); Hornbach et al. (2010); McHugh, Seeber, et al. (2014). The presence of (submarine) fault bends or step-overs is likely in a transtensional setting, yet estimates of slip distributions on such (sometimes relatively small and offshore) bends are largely lacking in the literature due to the absence of direct observations. Therefore, it is likely that their contribution to co-seismic vertical displacements has often been overlooked. We demonstrate for Palu Bay that significant co-seismic uplift occurred offshore on a restraining fault bend, whereas the breath of geodetic observations do not show large vertical displacements onshore on either side of Palu Bay. Our inferred fault model then produces a signature that can explain a large majority of the tsunami observations, without the need to invoke a predominance for (submarine) landslide activity. Our study concurs with Tinti et al. (2006) in suggesting that fault bends and step-overs may play a large role in generating tsunamis in transtensional basins, whereas (submarine) landslide contributions complement the picture locally.

9 Conclusions

Based on our integration of GPS and SAR co-seismic displacements, we conclude that the continuous, 3D, co-seismic displacement field resolves many features of the 2018 Palu earthquake. This includes a sharp surface rupture in Palu Valley, but an absence of a displacement discontinuity in the Sulawesi Neck. The observations are consistent with a continuous left-lateral strike-slip fault system. We interpret the geodetic data with a Bayesian fault inversion, and observe a number of fault bends and a secondary fault in the Sulawesi Neck that we attribute to normal faulting. The Palu-Koro Fault is a continuous and single near-vertical fault below $\sim$7 km depth, that branches into multiple semi-parallel fault segments towards shallower depth levels. A strike of 350° for the deep part of the fault underlying the shallow faults forming the 2018 rupture is consistent with the orientations of faults in the Palu-Koro fault region, and with interseismic velocities. Still, we find that most of the slip occurred at shallow (< 7 km) depths. The magnitude of displacement is generally larger east of the fault, and our inversion suggests for most segments a dip angle in the range 45-50°.

The observed fault bends and the inferred fault bend underneath Palu Bay conform to our interpretation of the tectonic setting as a transtensional basin. Our observations suggest transtensional co-seismic subsidence as well as transpressional uplift on shallow fault bends. The fault bends that connect the straight, dominantly strike-slip segments of the rupture have accommodated significant dip-slip motion during the earthquake. Below the bay, our model predicts uplift of the sea floor up to 2-3 m due to dip-slip on an inferred fault bend, which connects the northern fault segment in the Sulawesi Neck and the approximately parallel fault segment south in Palu Valley.

Combining the inversion results with a tsunami model, we conclude that the tsunami arrival times and wave polarity from amateur and CCTV videos in the south and south-eastern part of the bay can be described with a co-seismic uplift source in the Bay. The modeled tsunami, based on the finite fault, produces a spatial distribution and magnitude of runup that is close to the survey data along the coastline of Palu Bay. From the various tested fault geometry scenarios below the Bay, the comparison of the model with tsunami data favors a relatively southerly location in the Bay. While the majority of tsunami observations can be explained by fault slip alone, the observed timing of the tsunami and the runup around Pantoloan and Wani are difficult to match with a co-seismic source, and are possibly caused by non-tectonic bathymetry changes. Irrespective of local effects, our data and modeling indicate that fault bends have played a major role in the tsunamigenesis of the 2018 Palu earthquake; fault bends may be equally important to consider for tsunami hazards in comparable strike-slip settings.

10 Open Research

The data underlying this manuscript and model results are available at the 4TU Research data repository (https://data.4tu.nl) (data will be made available upon acceptance, and conveyed to reviewers upon request). These data and results include: the GPS kinematic time series, GPS co-seismic displacement tables, the SAR displacement fields (quadtree), 3D displacement field estimate, finite fault solution (median solution for each fault scenario), bathymetry, time series of modeled inundation tsunami height at the six coastal sites and fields of tsunami elevation of scenario *IV*. The satellite imagery that we use to estimate tsunami inundation is available at: https://www.maxar.com/open-data/indonesia-earthquake-tsunami. We have made use of colormaps by Colorbrewer and Fabio Crameri (Crameri, 2018).

The software for this study is partly open access, as specified below:

- QGIS as used for the analysis of tsunami inundation is open access software (https://www.qgis.org).
- A research license for the GPS processing software GIPSY-OASIS II can be obtained at https://gipsy-oasis.jpl.nasa.gov.
- The Geodetic Bayesian Inversion Software GBIS is written in Matlab and is freely accessible at https://comet.nerc.ac.uk/downloadgbis.
- H2Ocean is open source software and will be made available upon request.
- The Matlab scripts to perform the displacement inversion can be obtained on request.
- GSISAR used for SAR processing is not accessible to the public or research community under the policy of GSI.

Acknowledgments

Author contributions following the CReDiT taxonomy:

Conceptualization: T.B. W.S. N.N. A.H. J.P. R.G. M.H. C.V.
Data Curation: W.S. D.A.S. J.E. S. C.V.
Formal analysis W.S. Y.M. D.A.S. M.N. J.E.
Funding acquisition: W.S. R.R. T.B. N.N. J.P. J.E. P.V. C.V.
Investigation: T.B. L.S. O.K. N.N. W.S. S.L. M.H.
Methodology: L.S. T.B. O.K. S.L.
f Project administration: W.S. H.A. J.E. G.H.P. C.H. P.V.
Resources : W.S. C.V. J.E. S.S. D.A.S. S.
Software: T.B. L.S. M.N.
Supervision: T.B. A.H. J.P. R.R.
Visualization: T.B. L.S. N.N. O.K. W.S.
Writing - original draft: T.B. N.N. W.S. L.S. Y.M. O.K. M.N. S.L. A.H.

Writing - review & editing T.B. N.N. R.G. R.R. P.V. A.H. W.S. J.P. C.V. Y.M. S.L. G.H.P.

Some specifications to the CReDiT contributions. Data curation concerns collecting GPS data and maintaining the GPS network. For the formal analysis, W.S. has processed the GPS data and Y.M. has performed the SAR-data processing; W.S. and M.N. combined bathymetric and topographic data. T.B. has led the investigation process and has combined the different co-seismic displacement datasets into the combined displacement field; L.S. has conducted the finite fault inversion; O.K. has performed the tsunami modeling; N.N. has analyzed the fault directions; S.L. has analyzed the inundation on basis of optical data. T.B. has taken lead in writing the manuscript, supported by N.N..

The continued (long-term) operation of the GPS stations in Central Sulawesi has been co-facilitated by the EU-ASEAN SEAMERGES (2004-2006) and GEO2TECDI-1/2 projects (2009-2013). The GPS data acquisition and research were also partly funded by grants from the Dutch NWO User Support Programme Space Research (2007-2023). A special thanks to our local survey staff Rahman Umar and Urip for their continued support, including the inspection of the GPS stations directly after the earthquake. ALOS-2 data were provided under a cooperative research contract between GSI and JAXA. The ownership of ALOS-2 data belongs to JAXA.

Taco Broerse is funded by NWO grant ALWGO.2018.038. Olga Kleptsova was initially funded by a 2 month PD grant awarded to J. Pietrzak by the Department of Hydraulic Engineering, TU Delft which is gratefully acknowledged. Matthew Herman was funded by The Netherlands Research Centre For Integrated Solid Earth Science, grant ISES 2017-UU-22. COMET is the UK Natural Environment Research Council's Centre for the Observation and Modelling of Earthquakes, Volcanoes and Tectonics.

References

Abendanon, E. (1915). Geologische en geografische doorkruizingen van Midden Celebes. *Bd. I–IV, Leiden*.

Aksu, A. E., Calon, T. J., Hiscott, R. N., & Yasar, D. (2000). Anatomy of the North Anatolian Fault Zone in the Marmara Sea, Western Turkey: extensional basins above a continental transform. *Gsa Today*, *10*(6), 3–7.

Altamimi, Z., Rebischung, P., Métivier, L., & Collilieux, X. (2016). ITRF2014: A new release of the International Terrestrial Reference Frame modeling nonlinear station motions. *Journal of Geophysical Research: Solid Earth*, *121*(8), 6109–6131.

Altınok, Y., Alpar, B., Özer, N., & Aykurt, H. (2011). Revision of the tsunami catalogue affecting Turkish coasts and surrounding regions. *Natural Hazards and Earth System Sciences*, *11*(2), 273–291.

Altınok, Y., & Ersoy, Ş. (2000). Tsunamis observed on and near the Turkish coast. In *Natural hazards* (pp. 185–205). Springer. doi: https://doi.org/10.1007/978-94-017-2386-2_5

Amey, R., Hooper, A., & Walters, R. (2018). A bayesian method for incorporating self-similarity into earthquake slip inversions. *Journal of Geophysical Research: Solid Earth*, *123*(7), 6052–6071.

Arikawa, T., Muhari, A., Okumura, Y., Dohi, Y., Afriyanto, B., Sujatmiko, K. A., & Imamura, F. (2018). Coastal Subsidence Induced Several Tsunamis During the 2018 Sulawesi Earthquake. *Journal of Disaster Research*, *13*.

Bacques, G., de Michele, M., Foumelis, M., Raucoules, D., Lemoine, A., & Briole, P. (2020). Sentinel optical and SAR data highlights multi-segment faulting during the 2018 Palu-Sulawesi earthquake (M w 7.5). *Scientific Reports*, *10*(1), 1–11. doi: https://doi.org/10.1038/s41598-020-66032-7

Bagnardi, M., & Hooper, A. (2018). Inversion of surface deformation data for rapid

estimates of source parameters and uncertainties: A Bayesian approach. *Geochemistry, Geophysics, Geosystems*, *19*(7), 2194–2211.

Bao, H., Ampuero, J.-P., Meng, L., Fielding, E. J., Liang, C., Milliner, C. W., ... Huang, H. (2019). Early and persistent supershear rupture of the 2018 magnitude 7.5 Palu earthquake. *Nature Geoscience*, *12*(3), 200–205.

Baran, I., Stewart, M. P., Kampes, B. M., Perski, Z., & Lilly, P. (2003). A modification to the Goldstein radar interferogram filter. *IEEE Transactions on Geoscience and Remote Sensing*, *41*(9), 2114-2118. doi: https://doi.org/10.1109/TGRS.2003.817212

Bechor, N. B. D., & Zebker, H. A. (2006). Measuring two-dimensional movements using a single InSAR pair. *Geophysical Research Letters*, *33*(16). doi: https://doi.org/10.1029/2006GL026883

Beck, C., Campos, C., Eriş, K., Çağatay, N., Mercier de Lepinay, B., & Jouanne, F. (2015). Estimation of successive coseismic vertical offsets using coeval sedimentary events–application to the southwestern limit of the Sea of Marmara's Central Basin (North Anatolian Fault). *Natural Hazards and Earth System Sciences*, *15*(2), 247–259. doi: https://doi.org/10.5194/nhess-15-247-20

Bellier, O., Beaudouin, T., Sebrier, M., Villeneuve, M., Bahar, I., Putranto, E., ... Seward, D. (1998). Active faulting in central Sulawesi (eastern Indonesia). *GEODYSSEA Project Final Report*, 98–14.

Bellier, O., Sébrier, M., Beaudouin, T., Villeneuve, M., Braucher, R., Bourles, D., ... Pratomo, I. (2001). High slip rate for a low seismicity along the Palu-Koro active fault in central Sulawesi (Indonesia). *Terra Nova*, *13*(6), 463–470.

Bellier, O., Sébrier, M., Seward, D., Beaudouin, T., Villeneuve, M., & Putranto, E. (2006). Fission track and fault kinematics analyses for new insight into the Late Cenozoic tectonic regime changes in West-Central Sulawesi (Indonesia). *Tectonophysics*, *413*(3-4), 201–220.

Bertiger, W., Desai, S. D., Haines, B., Harvey, N., Moore, A. W., Owen, S., & Weiss, J. P. (2010). Single receiver phase ambiguity resolution with GPS data. *Journal of Geodesy*, *84*(5), 327–337.

Bertrand, S., Doner, L., Akçer Ön, S., Sancar, U., Schudack, U., Mischke, S., ... Leroy, S. A. (2011). Sedimentary record of coseismic subsidence in Hersek coastal lagoon (Izmit Bay, Turkey) and the late Holocene activity of the North Anatolian Fault. *Geochemistry, Geophysics, Geosystems*, *12*(6). doi: https://doi.org/10.1029/2011GC003511

Biasi, G. P., & Wesnousky, S. G. (2016). Steps and gaps in ground ruptures: Empirical bounds on rupture propagation. *Bulletin of the Seismological Society of America*, *106*(3), 1110–1124. doi: https://doi.org/10.1785/0120150175

Bos, M., & Scherneck, H. (2014). *Onsala Space Observatory.* Retrieved from `http://holt.oso.chalmers.se/loading.Accessed1Mar2018`

Bradley, K., Mallick, R., Andikagumi, H., Hubbard, J., Meilianda, E., Switzer, A., ... others (2019). Earthquake-triggered 2018 Palu Valley landslides enabled by wet rice cultivation. *Nature Geoscience*, *12*(11), 935–939.

Çağatay, M., Erel, L., Bellucci, L., Polonia, A., Gasperini, L., Eriş, K., ... others (2012). Sedimentary earthquake records in the İzmit gulf, sea of Marmara, Turkey. *Sedimentary Geology*, *282*, 347–359. doi: https://doi.org/10.1016/j.sedgeo.2012.10.001

Carvajal, M., Araya-Cornejo, C., Sepúlveda, I., Melnick, D., & Haase, J. S. (2019). Nearly-instantaneous tsunamis following the Mw 7.5 2018 Palu earthquake. *Geophysical Research Letters*.

Cipta, A., Robiana, R., Griffin, J., Horspool, N., Hidayati, S., & Cummins, P. R. (2017). A probabilistic seismic hazard assessment for Sulawesi, Indonesia. *Geological Society, London, Special Publications*, *441*(1), 133–152.

Cormier, M.-H., Seeber, L., McHugh, C. M., Polonia, A., Çagatay, N., Emre, Ö., ... others (2006). North Anatolian Fault in the Gulf of Izmit (Turkey):

Rapid vertical motion in response to minor bends of a nonvertical continental transform. *Journal of Geophysical Research: Solid Earth*, *111*(B4). doi: https://doi.org/10.1029/2005JB003633

Crameri, F. (2018). Scientific colour-maps. doi: http://doi.org/10.5281/zenodo.1243862

Crowell, J. (1974). Origin of Late Cenozoic basins in southern California: Society of Economic Paleontologists and Mineralogists Special Publication No. 22.

Cui, H., Pietrzak, J., & Stelling, G. (2010). A finite volume analogue of the P1NC-P1 finite element: With accurate flooding and drying. *Ocean Modelling*, *35*(1), 16 - 30. doi: https://doi.org/10.1016/j.ocemod.2010.06.001

Cui, H., Pietrzak, J., & Stelling, G. (2012). Improved efficiency of a non-hydrostatic, unstructured grid, finite volume model. *Ocean Modelling*, *54-55*, 55 - 67. doi: https://doi.org/10.1016/j.ocemod.2012.07.001

Decriem, J., Árnadóttir, T., Hooper, A., Geirsson, H., Sigmundsson, F., Keiding, M., ... others (2010). The 2008 May 29 earthquake doublet in SW Iceland. *Geophysical Journal International*, *181*(2), 1128–1146.

Drab, L., Hubert Ferrari, A., Schmidt, S., & Martinez, P. (2012). The earthquake sedimentary record in the western part of the Sea of Marmara, Turkey. *Natural Hazards and Earth System Sciences*, *12*(4), 1235–1254. doi: https://doi.org/10.5194/nhess-12-1235-2012

Elbanna, A., Abdelmeguid, M., Ma, X., Amlani, F., Bhat, H. S., Synolakis, C., & Rosakis, A. J. (2021). Anatomy of strike-slip fault tsunami genesis. *Proceedings of the National Academy of Sciences*, *118*(19).

Fang, J., Xu, C., Wen, Y., Wang, S., Xu, G., Zhao, Y., & Yi, L. (2019). The 2018 Mw 7.5 Palu Earthquake: A Supershear Rupture Event Constrained by InSAR and Broadband Regional Seismograms. *Remote Sensing*, *11*(11), 1330.

Frucht, E., Salamon, A., Gal, E., Ginat, H., Grigorovitch, M., Tov, R. S., & Ward, S. (2019). A Fresh View of the Tsunami Generated by the Dead Sea Transform, 1995 Mw 7.2 Nuweiba Earthquake, along the Gulf of Elat–Aqaba. *Seismological Research Letters*, *90*(4), 1483–1493. doi: https://doi.org/10.1785/0220190004

Geist, E. L., & Parsons, T. (2005). Triggering of tsunamigenic aftershocks from large strike-slip earthquakes: Analysis of the November 2000 New Ireland earthquake sequence. *Geochemistry, Geophysics, Geosystems*, *6*(10). doi: https://doi.org/10.1029/2005GC000935

Geist, E. L., & Zoback, M. L. (1999). Analysis of the tsunami generated by the Mw 7.8 1906 San Francisco earthquake. *Geology*, *27*(1), 15–18. doi: https://doi.org/10.1130/0091-7613(1999)027⟨0015:AOTTGB⟩2.3.CO;2

Goda, K., Mori, N., Yasuda, T., Prasetyo, A., Muhammad, A., & Tsujio, D. (2019). Cascading geological hazards and risks of the 2018 Sulawesi Indonesia earthquake and sensitivity analysis of tsunami inundation simulations. *Frontiers in Earth Science*, *7*, 261. doi: https://doi.org/10.3389/feart.2019.00261

Goldstein, R. M., & Werner, C. L. (1998). Radar interferogram filtering for geophysical applications. *Geophysical Research Letters*, *25*(21), 4035-4038. doi: https://doi.org/10.1029/1998GL900033

Gomba, G., Parizzi, A., De Zan, F., Eineder, M., & Bamler, R. (2016). Toward operational compensation of ionospheric effects in SAR interferograms: The split-spectrum method. *IEEE Transactions on Geoscience and Remote Sensing*, *54*(3), 1446-1461. doi: https://doi.org/10.1109/TGRS.2015.2481079

Gusman, A. R., Satake, K., & Harada, T. (2017). Rupture process of the 2016 Wharton Basin strike-slip faulting earthquake estimated from joint inversion of teleseismic and tsunami waveforms. *Geophysical Research Letters*, *44*(9), 4082–4089. doi: https://doi.org/10.1002/2017GL073611

Gusman, A. R., Supendi, P., Nugraha, A. D., Power, W., Latief, H., Sunendar, H., ... others (2019). Source Model for the Tsunami Inside Palu Bay Following

the 2018 Palu Earthquake, Indonesia. *Geophysical Research Letters*, *46*(15), 8721–8730.

Harding, T. P. (1985). Seismic characteristics and identification of negative flower structures, positive flower structures, and positive structural inversion. *AAPG Bulletin*, *69*(4), 582–600.

Hastings, W. K. (1970). Monte Carlo sampling methods using Markov chains and their applications.

He, L., Feng, G., Li, Z., Feng, Z., Gao, H., & Wu, X. (2019). Source parameters and slip distribution of the 2018 Mw 7.5 Palu, Indonesia earthquake estimated from space-based geodesy. *Tectonophysics*, *772*, 228216. doi: https://doi.org/10.1016/j.tecto.2019.228216

Hébert, H., Schindele, F., Altınok, Y., Alpar, B., & Gazioglu, C. (2005). Tsunami hazard in the Marmara Sea (Turkey): a numerical approach to discuss active faulting and impact on the Istanbul coastal areas. *Marine Geology*, *215*(1-2), 23–43. doi: https://doi.org/10.1016/j.margeo.2004.11.006

Heidarzadeh, M., Muhari, A., & Wijanarto, A. B. (2019). Insights on the source of the 28 September 2018 Sulawesi tsunami, Indonesia based on spectral analyses and numerical simulations. *Pure and Applied Geophysics*, *176*(1), 25–43.

Heidbach, O., Rajabi, M., Cui, X., Fuchs, K., Müller, B., Reinecker, J., ... others (2018). The World Stress Map database release 2016: Crustal stress pattern across scales. *Tectonophysics*, *744*, 484–498. doi: https://doi.org/10.1016/j.tecto.2018.07.007

Hennig, J., Hall, R., Forster, M. A., Kohn, B. P., & Lister, G. S. (2017). Rapid cooling and exhumation as a consequence of extension and crustal thinning: Inferences from the Late Miocene to Pliocene Palu Metamorphic Complex, Sulawesi, Indonesia. *Tectonophysics*, *712*, 600–622.

Hooper, A., Pietrzak, J., Simons, W., Cui, H., Riva, R., Naeije, M., ... Socquet, A. (2013). Importance of horizontal seafloor motion on tsunami height for the 2011 Mw=9.0 Tohoku-Oki earthquake. *Earth and Planetary Science Letters*, *361*, 469 - 479. Retrieved from `http://www.sciencedirect.com/science/article/pii/S0012821X1200622X` doi: https://doi.org/10.1016/j.epsl.2012.11.013

Hornbach, M. J., Braudy, N., Briggs, R. W., Cormier, M.-H., Davis, M. B., Diebold, J. B., ... others (2010). High tsunami frequency as a result of combined strike-slip faulting and coastal landslides. *Nature Geoscience*, *3*(11), 783–788. doi: https://doi.org/10.1038/ngeo975

Imamura, F., Synolakis, C. E., Gica, E., Titov, V., Listanco, E., & Lee, H. J. (1995). Field survey of the 1994 Mindoro Island, Philippines tsunami. *pure and applied geophysics*, *144*(3-4), 875–890. doi: https://doi.org/10.1007/BF00874399

Jamelot, A., Gailler, A., Heinrich, P., Vallage, A., & Champenois, J. (2019). Tsunami simulations of the Sulawesi M w 7.5 event: Comparison of seismic sources issued from a tsunami warning context versus post-event finite source. *Pure and Applied Geophysics*, *176*(8), 3351–3376.

Jaya, A., Nishikawa, O., & Jumadil, S. (2019). Distribution and morphology of the surface ruptures of the 2018 Donggala–Palu earthquake, Central Sulawesi, Indonesia. *Earth, Planets and Space*, *71*(1), 1–13. doi: https://doi.org/10.1186/s40623-019-1126-3

Johnston, G., Riddell, A., & Hausler, G. (2017). The international GNSS service. In *Teunissen, peter j.g., and montenbruck, o. (eds.), springer handbook of global navigation satellite systems* (pp. 967–982). Springer. doi: https://doi.org/10.1007/978-3-319-42928-1

Jung, H. S., Won, J. S., & Kim, S. W. (2009). An improvement of the performance of multiple-aperture SAR interferometry (MAI) . *IEEE Transactions on Geoscience and Remote Sensing*, *47*(8), 2859-2869. doi: https://doi.org/10.1109/TGRS.2009.2016554

Katili, J. A. (1970). Large transcurrent faults in Southeast Asia with special reference to Indonesia. *Geologische Rundschau*, *59*(2), 581–600.

King, D. (2015). Tsunami hazard, assessment and risk in Aotearoa–New Zealand: a systematic review AD 1868–2012. *Earth-Science Reviews*, *145*, 25–42. doi: https://doi.org/10.1016/j.earscirev.2015.02.004

Kobayashi, T., Takada, Y., Furuya, M., & Murakami, M. (2009). Locations and types of ruptures involved in the 2008 Sichuan earthquake inferred from SAR image matching. *Geophysical Research Letters*, *36*(7). doi: https://doi.org/10.1029/2008GL036907

Laigle, M., Becel, A., de Voogd, B., Hirn, A., Taymaz, T., Ozalaybey, S., et al. (2008). A first deep seismic survey in the Sea of Marmara: Deep basins and whole crust architecture and evolution. *Earth and Planetary Science Letters*, *270*(3-4), 168–179. doi: https://doi.org/10.1016/j.epsl.2008.02.031

Latcharote, P., Suppasri, A., Imamura, F., Aytore, B., & Yalçıner, A. C. (2016). Possible worst-case tsunami scenarios around the Marmara Sea from combined earthquake and landslide sources. *Pure and Applied Geophysics*, *173*, 3823–3846. doi: https://doi.org/10.1007/s00024-016-1411-z

Lee, S.-J., Wong, T.-P., Lin, T.-C., & Liu, T.-Y. (2019). Complex Triggering Supershear Rupture of the 2018 M w 7.5 Palu, Indonesia, Earthquake Determined from Teleseismic Source Inversion. *Seismological Research Letters*, *90*(6), 2111–2120. doi: https://doi.org1/0.1785/0220190111

Leeuwen, T. M. v., & Muhardjo. (2005). Stratigraphy and tectonic setting of the Cretaceous and Paleogene volcanic-sedimentary successions in northwest Sulawesi, Indonesia: implications for the Cenozoic evolution of Western and Northern Sulawesi. *Journal of Asian Earth Sciences*, *25*(3), 481–511.

Lettis, W., Bachhuber, J., Witter, R., Brankman, C., Randolph, C., Barka, A., ... Kaya, A. (2002). Influence of releasing step-overs on surface fault rupture and fault segmentation: Examples from the 17 August 1999 Izmit earthquake on the North Anatolian fault, Turkey. *Bulletin of the Seismological Society of America*, *92*(1), 19–42.

Li, Q., Zhao, B., Tan, K., & Xu, W. (2020). Two main rupture stages during the 2018 magnitude 7.5 Sulawesi earthquake. *Geophysical Journal International*, *221*(3), 1873–1882.

Liu, P., Higuera, P., Husrin, S., Prasetya, G., Prihantono, J., Diastomo, H., ... Susmoro, H. (2020). Coastal landslides in Palu Bay during 2018 Sulawesi earthquake and tsunami. *Landslides*. doi: https://doi.org/10.1007/s10346-020-01417-3

Maeda, T., & Furumura, T. (2013). FDM simulation of seismic waves, ocean acoustic waves, and tsunamis based on tsunami-coupled equations of motion. *Pure and Applied Geophysics*, *170*(1), 109–127.

Maerten, F., Resor, P., Pollard, D., & Maerten, L. (2005). Inverting for slip on three-dimensional fault surfaces using angular dislocations. *Bulletin of the Seismological Society of America*, *95*(5), 1654–1665.

McHugh, C. M., Braudy, N., Çağatay, M. N., Sorlien, C., Cormier, M.-H., Seeber, L., & Henry, P. (2014). Seafloor fault ruptures along the North Anatolia Fault in the Marmara Sea, Turkey: Link with the adjacent basin turbidite record. *Marine Geology*, *353*, 65–83. doi: https://doi.org/10.1016/j.margeo.2014.03.005

McHugh, C. M., Seeber, L., Cormier, M.-H., & Hornbach, M. (2014). Submarine Paleoseismology along populated transform boundaries: the Enriquillo-plantain-garden fault, Canal du Sud, Haiti, and the north Anatolian fault, Marmara Sea, Turkey. *Oceanography*, *27*(2), 118–131. doi: https://doi.org/10.5670/oceanog.2014.47

Metropolis, N., Rosenbluth, A. W., Rosenbluth, M. N., Teller, A. H., & Teller, E. (1953). Equation of state calculations by fast computing machines. *The*

journal of chemical physics, *21*(6), 1087–1092.

Michel, R., Avouac, J. P., & Taboury, J. (1999). Measuring near field coseismic displacements from SAR images: application to the Landers earthquake. *Geophysical Research Letters*, *26*(19), 3017-3020. doi: https://doi.org/10.1029/1999GL900524

Mikami, T., Shibayama, T., Esteban, M., Takabatake, T., Nakamura, R., Nishida, Y., ... others (2019). Field survey of the 2018 Sulawesi tsunami: inundation and run-up heights and damage to coastal communities. *Pure and Applied Geophysics*, *176*(8), 3291–3304.

Morishita, Y., Kobayashi, T., & Yarai, H. (2016). Three-dimensional deformation mapping of a dike intrusion event in Sakurajima in 2015 by exploiting the right-and left-looking ALOS-2 InSAR. *Geophysical Research Letters*, *43*(9), 4197–4204.

Muhari, A., Imamura, F., Arikawa, T., Hakim, A. R., & Afriyanto, B. (2018). Solving the puzzle of the september 2018 Palu, Indonesia, tsunami mystery: Clues from the tsunami waveform and the initial field survey data. *Journal of Disaster Research*, *13*.

Mustafar, M. A., Simons, W. J., Tongkul, F., Satirapod, C., Omar, K. M., & Visser, P. N. (2017). Quantifying deformation in North Borneo with GPS. *Journal of Geodesy*, *91*(10), 1241–1259.

Nakata, K., Katsumata, A., & Muhari, A. (2020). Submarine landslide source models consistent with multiple tsunami records of the 2018 Palu tsunami, Sulawesi, Indonesia. *Earth, Planets and Space*, *72*, 1–16.

Natawidjaja, D. H., Daryono, M. R., Prasetya, G., Liu, P. L., Hananto, N. D., Kongko, W., ... others (2020). The 2018 Mw7. 5 Palu supershear earthquake ruptures geological fault's multi-segment separated by large bends: Results from integrating field measurements, LiDAR, swath bathymetry, and seismic-reflection data. *Geophysical Journal International*. doi: https://doi.org/10.1093/gji/ggaa498

Nijholt, N., Simons, W., Efendi, J., Sarsito, D., & Riva, R. (2021). A transient in surface motions dominated by deep afterslip subsequent to a shallow supershear earthquake: The 2018 Mw7. 5 Palu Case. *Geochemistry, Geophysics, Geosystems*, *22*(4), e2020GC009491. doi: https://doi.org/10.1029/2020GC009491

Oglesby, D. D. (2005). The dynamics of strike-slip step-overs with linking dip-slip faults. *Bulletin of the Seismological Society of America*, *95*(5), 1604–1622.

Ohmachi, T., Tsukiyama, H., & Matsumoto, H. (2001). Simulation of tsunami induced by dynamic displacement of seabed due to seismic faulting. *Bulletin of the Seismological Society of America*, *91*(6), 1898–1909.

Okada, Y. (1985). Surface deformation due to shear and tensile faults in a half-space. *Bulletin of the seismological society of America*, *75*(4), 1135–1154.

Omira, R., Dogan, G., Hidayat, R., Husrin, S., Prasetya, G., Annunziato, A., ... Yalciner, A. C. (2019). The September 28th, 2018, Tsunami In Palu-Sulawesi, Indonesia: A Post-Event Field Survey. *Pure and Applied Geophysics*, *176*(4), 1379-1395. doi: https://doi.org/10.1007/s00024-019-02145-z

Özaksoy, V., Emre, Ö., Yıldırım, C., Doğan, A., Özalp, S., & Tokay, F. (2010). Sedimentary record of late Holocene seismicity and uplift of Hersek restraining bend along the North Anatolian Fault in the Gulf of İzmit. *Tectonophysics*, *487*(1-4), 33–45. doi: https://doi.org/10.1016/j.tecto.2010.03.006

Öztürk, H., Koral, H., & Geist, E. (2000). Intra-basinal water movements induced by faulting: the August 17, 1999, Gölcük (İzmit Bay) earthquake (Mw= 7.4). *Marine Geology*, *170*(3-4), 263–270. doi: https://doi.org/10.1016/S0025-3227(00)00090-6

Pakoksung, K., Suppasri, A., Imamura, F., Athanasius, C., Omang, A., & Muhari, A. (2019). Simulation of the Submarine Landslide Tsunami on 28 September

2018 in Palu Bay, Sulawesi Island, Indonesia, Using a Two-Layer Model. *Pure and Applied Geophysics*, 1–28.

Patria, A., & Putra, P. S. (2020). Development of the Palu–Koro Fault in NW Palu Valley, Indonesia. *Geoscience Letters*, *7*(1), 1–11. doi: https://doi.org/10.1186/s40562-020-0150-2

Pelinovsky, E., Yuliadi, D., Prasetya, G., & Hidayat, R. (1997). The 1996 Sulawesi tsunami. *Natural Hazards*, *16*(1), 29–38.

Persson, P.-O., & Strang, G. (2004). A simple mesh generator in MATLAB. *SIAM review*, *46*(2), 329–345.

Poupardin, A., Calais, E., Heinrich, P., Hébert, H., Rodriguez, M., Leroy, S., ... Douilly, R. (2020). Deep Submarine Landslide Contribution to the 2010 Haiti Earthquake Tsunami. *Natural Hazards and Earth System Sciences*. doi: doi:10.5194/nhess-2019-388

Prasetya, G., De Lange, W., & Healy, T. (2001). The Makassar Strait tsunamigenic region, Indonesia. *Natural Hazards*, *24*(3), 295–307.

Putra, P. S., Aswan, A., Maryunani, K. A., Yulianto, E., & Kongko, W. (2019). Field Survey of the 2018 Sulawesi Tsunami Deposits. *Pure and Applied Geophysics*, 1–11.

Rabinovich, A. B., Thomson, R. E., Titov, V. V., Stephenson, F. E., & Rogers, G. C. (2008). Locally generated tsunamis recorded on the coast of British Columbia. *Atmosphere-Ocean*, *46*(3), 343–360. doi: https://doi.org/10.3137/ao.460304

Rebischung, P., & Schmid, R. (2016). IGS14/igs14. atx: a new framework for the IGS products. In *Agu fall meeting 2016.*

Roberts, K. J., Pringle, W. J., & Westerink, J. J. (2019). OceanMesh2D 1.0: MATLAB-based software for two-dimensional unstructured mesh generation in coastal ocean modeling. *Geoscientific Model Development*, *12*(5), 1847–1868. Retrieved from `https://www.geosci-model-dev.net/12/1847/2019/` doi: 10.5194/gmd-12-1847-2019

Rosen, P. A., Hensley, S., Zebker, H. A., Webb, F. H., & Fielding, E. J. (1996). Surface deformation and coherence measurements of Kilauea Volcano, Hawaii, from SIR-C radar interferometry. *Journal of Geophysical Research: Planets*, *101*(E10), 23109-23125. doi: https://doi.org/10.1029/96JE01459

Sassa, S., & Takagawa, T. (2019). Liquefied gravity flow-induced tsunami: first evidence and comparison from the 2018 Indonesia Sulawesi earthquake and tsunami disasters. *Landslides*, *16*(1), 195–200. doi: https://doi.org/10.1007/s10346-018-1114-x

Schambach, L., Grilli, S., & Tappin, D. (2020). New high-resolution modeling of the 2018 Palu tsunami, based on supershear earthquake mechanisms and mapped coastal landslides, supports a dual source. *Frontiers in Earth Science*, *8*, 627. doi: https://doi.org/10.3389/feart.2020.598839

Sepúlveda, I., Haase, J. S., Carvajal, M., Xu, X., & Liu, P. L. (2020). Modeling the sources of the 2018 Palu, Indonesia, tsunami using videos from social media. *Journal of Geophysical Research: Solid Earth*, *125*(3), e2019JB018675. doi: https://doi.org/10.1029/2019JB018675

Shimozono, T., Cui, H., Pietrzak, J., Fritz, H., Okayasu, A., & Hooper, A. (2014). Short Wave Amplification and Extreme Runup by the 2011 Tohoku Tsunami. *Pure & Applied Geophysics*, *171*(12), 3217 - 3228.

Simons, W., Socquet, A., Vigny, C., Ambrosius, B., Haji Abu, S., Promthong, C., ... others (2007). A decade of GPS in Southeast Asia: Resolving Sundaland motion and boundaries. *J. Geophys. Res.*, *112*(B6).

Socquet, A., Hollingsworth, J., Pathier, E., & Bouchon, M. (2019). Evidence of supershear during the 2018 magnitude 7.5 Palu earthquake from space geodesy. *Nature Geoscience*, *12*(3), 192.

Socquet, A., Simons, W., Vigny, C., McCaffrey, R., Subarya, C., Sarsito, D., ... Spakman, W. (2006). Microblock rotations and fault coupling in SE Asia triple junction (Sulawesi, Indonesia) from GPS and earthquake slip vector data. *Journal of Geophysical Research: Solid Earth*, *111*(B8).

Sotiris, V., Athanassios, G., Varvara, T., & Aggeliki, B. (2018, October). *A preliminary report on the M7.5 Palu 2018 earthquake co-seismic ruptures and landslides using image correlation techniques on optical satellite data.* Retrieved from `https://doi.org/10.5281/zenodo.1467128` (Report submitted to EMSC on 19 October 2018 12:00 UTC) doi: 10.5281/zenodo.1467128

Stevens, C., McCaffrey, R., Bock, Y., Genrich, J., Subarya, C., Puntodewo, S., & Vigny, C. (1999). Rapid rotations about a vertical axis in a collisional setting revealed by the Palu fault, Sulawesi, Indonesia. *Geophysical Research Letters*, *26*(17), 2677–2680.

Supendi, P., Nugraha, A. D., Widiyantoro, S., Abdullah, C. I., Puspito, N. T., Palgunadi, K. H., ... Wiyono, S. H. (2019). Hypocenter relocation of the aftershocks of the Mw 7.5 Palu earthquake (September 28, 2018) and swarm earthquakes of Mamasa, Sulawesi, Indonesia, using the BMKG network data. *Geoscience Letters*, *6*(1), 1–11.

Supendi, P., Nugraha, A. D., Widiyantoro, S., Pesicek, J. D., Thurber, C., Abdullah, C., ... Rosalia, S. (2020). Relocated aftershocks and background seismicity in eastern Indonesia shed light on the 2018 Lombok and Palu earthquake sequences. *Geophysical Journal International*, *221*(3), 1845–1855. doi: https://doi.org/10.1093/gji/ggaa118

Switzer, A. D., Majewski, J. M., Guan, R. Y., Benazir, B., Meilianda, E., Parham, P. R., ... Horton, B. P. (2019). The tsunami deposits of the September 28, 2018 Palu earthquake, Sulawesi, Indonesia. *Geophysical Research Abstracts*, *21*. (EGU2019-6290)

Syamsidik, Benazir, Umar, M., Margaglio, G., & Fitrayansyah, A. (2019). Post-tsunami survey of the 28 September 2018 tsunami near Palu Bay in Central Sulawesi, Indonesia: Impacts and challenges to coastal communities. *International Journal of Disaster Risk Reduction*, *38*, 101229.

Takagi, H., Pratama, M. B., Kurobe, S., Esteban, M., Aránguiz, R., & Ke, B. (2019). Analysis of generation and arrival time of landslide tsunami to Palu City due to the 2018 Sulawesi earthquake. *Landslides*, 1–9. doi: https://doi.org/10.1007/s10346-019-01166-y

Tanioka, Y., & Satake, K. (1996). Tsunami generation by horizontal displacement of ocean bottom. *Geophys. Res. Lett.*, *23*, 861–864.

Tchalenko, J. (1970). Similarities between shear zones of different magnitudes. *Geological Society of America Bulletin*, *81*(6), 1625–1640. doi: https://doi.org/10.1130/0016-7606(1970)81[1625:SBSZOD]2.0.CO;2

ten Brink, U., Wei, Y., Fan, W., Granja-Bruña, J.-L., & Miller, N. (2020). Mysterious tsunami in the Caribbean Sea following the 2010 Haiti earthquake possibly generated by dynamically triggered early aftershocks. *Earth and Planetary Science Letters*, *540*, 116269. doi: https://doi.org/10.1016/j.epsl.2020.116269

Tinti, S., Armigliato, A., Manucci, A., Pagnoni, G., Zaniboni, F., Yalçiner, A. C., & Altınok, Y. (2006). The generating mechanisms of the August 17, 1999 Izmit bay (Turkey) tsunami: regional (tectonic) and local (mass instabilities) causes. *Marine Geology*, *225*(1-4), 311–330. doi: https://doi.org/10.1016/j.margeo.2005.09.010

Tobita, M., Murakami, M., Nakagawa, H., Yarai, H., Fujiwara, S., & Rosen, P. A. (2001). 3-D surface deformation of the 2000 Usu eruption measured by matching of SAR images. *Geophysical Research Letters*, *28*(22), 4291-4294. doi: https://doi.org/10.1029/2001GL013329

Ulrich, T., Vater, S., Madden, E. H., Behrens, J., van Dinther, Y., Van Zelst, I., ... Gabriel, A.-A. (2019). Coupled, physics-based modeling reveals earthquake dis-

placements are critical to the 2018 Palu, Sulawesi Tsunami. *Pure and Applied Geophysics*, *176*(10), 4069–4109.

USGS. (2018). *Finite fault solution of the Mw 7.5 Palu earthquake, Indonesia. US Geological Survey.* Retrieved 2021-5-4, from `https://earthquake.usgs.gov/earthquakes/eventpage/us1000h3p4/finite-fault`

Van Laarhoven, P. J., & Aarts, E. H. (1987). Simulated annealing. In *Simulated annealing: Theory and applications* (pp. 7–15). Springer.

Vigny, C., Perfettini, H., Walpersdorf, A., Lemoine, A., Simons, W., van Loon, D., ... others (2002). Migration of seismicity and earthquake interactions monitored by GPS in SE Asia triple junction: Sulawesi, Indonesia. *Journal of Geophysical Research: Solid Earth*, *107*(B10), ETG–7.

Walpersdorf, A., Rangin, C., & Vigny, C. (1998). GPS compared to long-term geologic motion of the north arm of Sulawesi. *Earth and Planetary Science Letters*, *159*(1-2), 47–55.

Walpersdorf, A., Vigny, C., Subarya, C., & Manurung, P. (1998). Monitoring of the Palu-Koro Fault (Sulawesi) by GPS. *Geophysical Research Letters*, *25*(13), 2313–2316.

Wang, H., & Wright, T. (2012). Satellite geodetic imaging reveals internal deformation of western Tibet. *Geophysical Research Letters*, *39*(7).

Wang, Y., Feng, W., Chen, K., & Samsonov, S. (2019). Source characteristics of the 28 September 2018 Mw 7.4 Palu, Indonesia, earthquake derived from the advanced land observation satellite 2 data. *Remote Sensing*, *11*(17), 1999.

Watkinson, I. M., & Hall, R. (2017). Fault systems of the eastern Indonesian triple junction: evaluation of Quaternary activity and implications for seismic hazards. *Geological Society, London, Special Publications*, *441*(1), 71–120.

Watkinson, I. M., & Hall, R. (2019). Impact of communal irrigation on the 2018 Palu earthquake-triggered landslides. *Nature Geoscience*, *12*(11), 940–945.

Widiyanto, W., Santoso, P. B., Hsiao, S.-C., & Imananta, R. T. (2019). Post-event field survey of 28 September 2018 Sulawesi earthquake and tsunami. *Natural Hazards and Earth System Sciences*, *19*(12), 2781–2794. doi: https://doi.org/10.5194/nhess-19-2781-2019

Williamson, A. L., Melgar, D., Xu, X., & Milliner, C. (2020). The 2018 Palu Tsunami: Coeval Landslide and Coseismic Sources. *Seismological Research Letters*. doi: https://doi.org/10.1785/0220200009

Wilson, P., Rais, J., Reigber, C., Reinhart, E., Ambrosius, B., Le Pichon, X., ... others (1998). Study provides data on active plate tectonics in Southeast Asia region. *Eos, Transactions American Geophysical Union*, *79*(45), 545–549.

Wright, T. J., Parsons, B. E., & Lu, Z. (2004). Toward mapping surface deformation in three dimensions using InSAR. *Geophysical Research Letters*, *31*(1).

Wu, D., Ren, Z., Liu, J., Chen, J., Guo, P., Yin, G., ... Yang, X. (2020). Coseismic surface rupture during the 2018 Mw 7.5 Palu earthquake, Sulawesi Island, Indonesia. *GSA Bulletin*.

Yalçıner, A. C., Alpar, B., Altınok, Y., Özbay, İ., & Imamura, F. (2002). Tsunamis in the Sea of Marmara: Historical documents for the past, models for the future. *Marine Geology*, *190*(1-2), 445–463. doi: https://doi.org/10.1016/S0025-3227(02)00358-4

Yalçıner, A. C., Hidayat, R., Husrin, S., Prasetya, G., Annunziato, A., Doğan, G. G., ... Pelinovsky, E. (2018). *The 28th September 2018 Palu Earthquake and Tsunami ITST 07-11 November 2018 Post Tsunami Field Survey Report (Short).* Retrieved from `http://itic.ioc-unesco.org/images/stories/itst_tsunami_survey/itst_palu/ITST-Nov-7-11-Short-Survey-Report-due-on-November-23-2018.pdf`

Yamazaki, D., Ikeshima, D., Tawatari, R., Yamaguchi, T., O'Loughlin, F., Neal, J. C., ... Bates, P. (2017). A high-accuracy map of global terrain elevations. *Geophysical Research Letters*, *44*(11), 5844–5853. doi: https://doi.org/

10.1002/2017GL072874

Yolsal-Çevikbilen, S., & Taymaz, T. (2019). Source Characteristics of the 28 September 2018 M w 7.5 Palu-Sulawesi, Indonesia (SE Asia) Earthquake Based on Inversion of Teleseismic Bodywaves. *Pure and Applied Geophysics*, *176*(10), 4111–4126. doi: https://doi.org/10.1007/s00024-019-02294-1

Zhang, Y., Chen, Y.-T., & Feng, W. (2019). Complex multiple-segment ruptures of the 28 September 2018, Sulawesi, Indonesia, earthquake. *Science Bulletin*, *64*(10), 650–652.

Zumberge, J., Heflin, M., Jefferson, D., Watkins, M., & Webb, F. (1997). Precise point positioning for the efficient and robust analysis of GPS data from large networks. *Journal of geophysical research: solid earth*, *102*(B3), 5005–5017.